Earth Surf. Dynam. Discuss., https://doi.org/10.5194/esurf-2017-39
Manuscript under review for journal Earth Surf. Dynam.
Discussion started: 21 June 2017

Earth Surface Dynamics Discussions
Open Access
EGU

A hydro-climatological approach to predicting regional landslide probability using Landlab

Ronda Strauch[1], Erkan Istanbulluoglu[1], Sai Siddhartha Nudurupati[1], Christina Bandaragoda[1], Nicole M. Gasparini[2], and Gregory E. Tucker[3]

1. Civil and Environmental Engineering, University of Washington, Seattle, WA

2. Earth and Environmental Sciences, Tulane University, New Orleans, LA, USA

3. Cooperative Institute for Research in Environmental Sciences (CIRES) and Department of Geological Sciences, University of Colorado Boulder, Boulder, CO, USA

Corresponding to: Ronda Strauch (rstrauch@u.washington.edu)

Abstract

We develop a hydro-climatological approach to modeling of regional shallow landslide initiation that integrates spatial and temporal dimensions of parameter uncertainty to estimate an annual probability of landslide initiation. The physically-based model couples the infinite slope stability model with a steady-state subsurface flow representation and operates on a digital elevation model. Spatially distributed raster data for soil properties and a soil evolution model and vegetation classification from National Land Cover Data are used to derive parameters for probability distributions to represent input uncertainty. Hydrologic forcing to the model is through annual maximum recharge to subsurface flow obtained from a macroscale hydrologic model, routed on raster grid to develop subsurface flow. A Monte Carlo approach is used to generate model parameters at each grid cell and calculate probability of shallow landsliding. We demonstrate the model in a steep mountainous region in northern Washington, U.S.A., using 30-m grid resolution over 2,700 km^2. The influence of soil depth on the probability of landslide initiation is investigated through comparisons among model output produced using three different soil depth scenarios reflecting uncertainty of soil depth and its potential long-term variability. We found elevation dependent patterns in probability of landslide initiation that showed the stabilizing effects of forests in low elevations, an increased landslide probability with forest decline at mid elevations (1,400 to 2,400 m), and soil limitation and steep topographic controls at high alpine elevations and post-glacial landscapes. These dominant controls manifest in a bimodal distribution of spatial annual landslide probability. Model testing with limited observations revealed similar model confidence for the three hazard

maps, suggesting suitable use as relative hazard products. Validation of the model with observed landslides is hindered by the completeness and accuracy of the inventory, estimation of source areas, and unmapped landslides. The model is available as a component in Landlab, an open-source, Python-based landscape earth systems modeling environment, and is designed to be easily reproduced utilizing HydroShare cyberinfrastructure.

1 Introduction

In steep mountainous landscapes, episodic shallow landslides (generally <2 m depth; Bordoni et al, 2015) and landslide-triggered debris flows are often the dominant form of hillside erosion and major source of sediment into streams (Benda and Dunne, 1997a, b; Goode et al., 2012). Where landslide processes intersect with human development, they cause property damage, disruption of infrastructure, injury, and loss of life (Taylor and Brabb, 1986; Baum et al., 2008a), contribute to sedimentation in reservoirs (Bathurst et al., 2005), and may even lead to dam failures (Ghirotti, 2012). Landslides provide punctuated sediment input to streams, affecting stream geomorphology (Benda and Dunne, 1997a, 1997b) and ecosystem dynamics (Pollock, 1998; May et al., 2009). Landslide hazard maps are a common tool used to characterize the relative potential for landslide occurrence in space, either qualitatively (using susceptibility levels) or quantitatively (using modeled landslide probabilities) (van Westen et al., 2006; Raia et al., 2014).

Our objective is to develop a parsimonious probabilistic model of shallow landslide initiation that can be implemented with minimal calibration for landslide hazard mapping using regionally available, spatially distributed input data for soil, vegetation type, local topography, and hydroclimatology. Based on the literature review presented below, we propose that a regional landslide hazard model should: (1) be flexible enough to incorporate changes in intrinsic and extrinsic conditions, such as vegetation and climate; (2) account for spatial variability in model parameters and forcings, and (3) integrate spatial and temporal dimensions of uncertainty to quantify landslide probability. With these principles in mind, we develop a hydro-climatological approach to modeling regional landslide hazard using the Landlab (version 1.1.0) modeling toolkit - an open-source, Python-based earth surface modeling framework that provides flexible model customization and coupling (Hobley et al., 2017). Next, we provide a short literature review that guides the design of our landslide modeling approach.

1.1 Geomorphology and Modeling Background

Landslides occur when destabilizing forces due to gravity and pore-water pressure exceed the resisting forces of friction and cohesion over a failure plane. These forces are controlled by intrinsic hillslope conditions, including attributes of topography, such as local slope and upslope contributing area, and properties of rock, soil, and vegetation root cohesion; and extrinsic drivers of rainfall, snowmelt, and earthquakes (Crozier, 1986; Wu and Sidle, 1995; van Beek, 2002; Naudet et al., 2008). There are three primary components of a landslide: (1) a source area or landslide scar where the initial failure begins, (2) a transmission or scour zone, such as a debris flow channel, and (3) a toe or zone of deposition (Lu and Godt, 2013).

Landslide susceptibility can be identified through numerous methods, which can be broadly grouped into empirical methods and process-based numerical models (Hammond et al., 1992; Wu and Sidle, 1995; Sidle and Ochiai, 2006). Data-driven empirical approaches relate the number and frequency of historical landslide observations in a region to triggering events (Caine, 1980; Crozier, 1999; Glade, 2001), landscape attributes (Carrara et al., 1995; Chung et al., 1995; Lee et al., 2007), or a combination of both (Kirschbaum et al., 2012) using threshold relations and various statistical models such as logistic regression, fuzzy logic, artificial neural networks, and support vector machine (Lee et al., 2007; Pardeshi et al., 2013; Chen et al., 2014). Empirical methods have been used for landslide susceptibility zonation or categorizing the landscape into relative landslide hazards (Sidle and Ochiai 2006).

Process-based models employ effective stress principles to characterize the destabilizing and resisting forces under hydrologic drivers (Iverson, 2000; Montrasio and Valentino 2016), offering the ability to explore changes in environmental and climatic conditions. Such process-based models are especially useful in areas with limited landslide inventories (Pardeshi et al. 2013). Recent process-based numerical models have largely focused on improving the characterization of the space-time dynamics of subsurface flow as a driver of pore-water pressure (e.g., Baum et al., 2008b; Raia et al., 2014; Anagnostopoulos et al., 2015; Montrasio and Valentino, 2016). Distributed hydrology models that use steady-state or transient solutions for subsurface flow depth were coupled with an infinite-slope stability model that solves the ratio of stabilizing to destabilizing forces on a failure plane parallel to the land surface (Montgomery and Dietrich, 1994; Miller, 1995; Wu and Sidle, 1995; Pack et al., 1998; Borga et al., 1998; Casadei et al., 2003; Tarolli and Tarboton, 2006; Baum et al., 2008b).

Steady-state models assume that lateral subsurface flow, driven by the topographic gradient, at each point on the landscape is in equilibrium with a steady-state recharge rate (Montgomery and Dietrich, 1994; Pack et al., 1998). The degree of soil saturation is predicted proportional to the ratio of upslope contributing area to local slope, and a ratio of watershed recharge and local soil transmissivity, following TOPMODEL assumptions (Beven and Kirkby, 1979; O'Loughlin, 1986; Pack et al., 1998). More recent efforts have focused on the development of transient flow models in various complexities by coupling vertical infiltration and redistribution processes in the unsaturated zone, using the Richards equation for unsaturated flow (Richards, 1931) or its variants, with lateral flow parameterizations such as kinematic wave in 1- and 2-dimensions (Iverson, 2000; Casadei et al., 2003; Baum et al., 2008b; Godt and McKenna, 2008; Raia et al., 2014; Alvioli et al., 2014; Anagnostopoulos et al., 2015).

While transient flow models have contributed to improved understanding of the influence of weather forcing and temporal variability in precipitation on landslide initiation, they remain tools typically applied for relatively small-scale assessments (Iverson, 2000; Raia et al. 2014). Transient models require a large number of hydrologic soil and vegetation parameters that are highly variable, uncertain, and difficult to measure or estimate (Godt and McKenna 2008; Baum et al. 2008b). In addition, in most steep forested mountains where landslide risk is high,

presence of macropores due to connected root structures, biological activity, fractures, large clasts, and lenses, leads to preferential and funneled flows that violate the assumptions of most matrix-flow models (Nimmo, 2005; Sidle et al., 2001; Gabet et al., 2003; Beven and Germann 2013). Numerical solutions to flow equations also present a major computational bottleneck in large-scale applications for probabilistic quantification of landslide hazard.

Comparison of steady-state and transient models using case studies with known extreme rainfall events that caused widespread landsliding involve statistical model performance evaluation (Zizioli et al., 2013). While using transient hydrologic models provided slight improvements in the prediction of landslide locations, overall, statistical comparisons of model outputs between steady-state and transient models revealed fairly similar degrees of success (Gorsevski et al., 2006; Zizioli et al., 2013; Anagnostopoulos et al., 2015; Boroni et al., 2015; Formetta et al., 2016). In some applications, model complexity increased the accuracy of predicted landslide locations at the expense of overestimating instability on unsaturated hillslopes (e.g., Godt et al., 2008; Bellugi 2011). In other cases, model precision increased while accuracy decreased (Gorsevski et al., 2006).

Data uncertainty due to spatial and temporal variability of parameters continues to be one of the major challenges in predicting landslides over broad regions (Crozier, 1986; Sidle and Ochiai, 2006; van Westen et. al., 2006; Baum et al., 2014; Anagnostopoulos et al., 2015). These uncertainties and variabilities can develop from geological anomalies, inherent spatial heterogeneities in soil and vegetation properties and their changes over time, and sampling limitations (El-Ramly et al., 2002; Cho, 2007; Baum et al., 2014). Uncertainties in hydro-climate quantities, such as precipitation and recharge, are particularly pronounced in steep high mountain regions due to lack of observations and complex spatial and temporal atmospheric processes (Roe, 2005; Wayland et al., 2016). Designating landslide hazard as a probability, rather than an index, systematically accounts for uncertainty and variability in stability analysis (Hammond et al., 1992) and more appropriately represents complex systems (Berti et al., 2012). Currently, only limited process-based models account for data uncertainty in landslide hazard mapping (e.g., Pack et al., 1998; Raia et al.,2014).

Observations and model experiments suggest that the largest landslides are usually associated with the largest rainfall events (e.g., Page et al. 1994; Gorsevski et al., 2006). Considering that hillslope hydrology is more likely to attain equilibrium conditions during prolonged wet conditions (e.g., Barling et al., 1994; Borga et al., 2002), a steady-state representation of subsurface flow hydrology, coupled with a process-based infinite slope stability model is an efficient approach for predicting the likelihood of landslide hazard at regional scales.

Lastly, most landslide hazard methods disregard a temporal dimension over which landslide probability is defined (Wu and Sidle, 1995; van Westen et al, 2006). As a result of that, instead of using estimated probabilities directly in the form of return periods of observed landslides or expected values for risks resulting from landslides, models use probability estimates as relative indices (eg., Pack et al., 1998) that can be used for hazard zonation (Pardeshi et al., 2013). Lack

of temporal dimension limits the incorporation of model results into risks assessments and the decision-making processes in high-risk regions.

1.2 Approach Overview

We develop a process-based modeling approach for shallow landslide initiation that incorporates imprecisions and uncertainties in hydro-climatological forcing, soils, and land cover properties. Rather than predicting critical rainfall intensity necessary to destabilize hillslopes (Montgomery and Dietrich 1994) or a terrain stability index map (Pack et al. 2001, 2005), our approach aims to develop a spatially continuous probability of landslide *initiation* that can be updated as conditions and triggers evolve. The model evaluates the infinite slope stability equation at the scale of a grid cell from a Digital Elevation Model (DEM). Daily rate of recharge (i.e., flux of water entering saturated zone) can be provided by model users from a variety of grid resolutions from hydrologic models such as the Variable Infiltration Capacity (VIC) model (*Liang et al.* 1994) as used in our regional application, or assigned as parameters by the user. A "Source Tracking Algorithm" (STA) is developed to route spatially variable recharge fields, at the native resolution of a hydrology model, generically referred to as a Hydrology Source Domain (HSD), onto the grid resolution of slope stability calculations. Raster grids derived from soil texture and vegetation cover classes are used with look-up tables to estimate model parameters ranges obtained from the literature to quantify uncertainty. Through Monte Carlo simulation (Raia et al., 2014), we calculate the probability of landslide initiation at each landscape grid cell. Our probability is further refined by a geomorphic soil evolution model that estimates soil depth with greater spatial heterogeneity than conventional soil survey map units, which is critical for slope stability analysis (Dietrich et al., 1995). This soil evolution model estimates long-term soil depth based primarily on soil mass production and slope-dependent sediment transport rules.

Landslide probability calculations are written in Python as a Landlab LandslideProbability component (landlab.github.io, including User Manual). The STA is available as a Landlab utility. The landslide model is designed as a user-written "driver" within Jupyter Notebooks, where the workflow of model application is presented. The driver and data are deployed on HydroShare (www.hydroshare.org), an online collaboration environment for sharing data, models, and code (Horsburgh et al., 2016; Idaszak et al., 2016), and made available for cloud computing via HydroShare JupyterHub infrastructure using a web browser (see Sect. 2.5).

In this work we explore the questions (1) How does regional hydro-climatology influence the spatial patterns of shallow landslide initiation over large geographic scales? and (2) How does distributed soil depth influence the probabilistic nature of landslide initiation compared to coarse-scale, homogenous soil depth estimates? We demonstrate our approach in a mountainous region of Washington, USA. This Pacific Northwest (PNW) region is naturally susceptible to landslides because of high and intense rainfall, steep mountains, active tectonics, and geologic and glacial history (Nadim et al., 2006; Sidle and Ochiai, 2006). The Oso landslide, which occurred in the vicinity of our study area in 2014, resulting in 43 fatalities and over $50 million in economic losses, provides a solemn reminder of the hazard landslides present

Earth Surf. Dynam. Discuss., https://doi.org/10.5194/esurf-2017-39
Manuscript under review for journal Earth Surf. Dynam.
Discussion started: 21 June 2017

(Wartman et al., 2016). Although the Oso landslide was a deep-seated type, the greater frequency of shallow landslides affords utility and relevance to our model.

2 Methodology

2.1 Probabilistic approach to landslide initiation

Our approach is based on the infinite slope stability equation derived from the Mohr-Coulomb failure law that predicts the factor-of-safety (FS) stability index of a hillslope parcel from the ratio of stabilizing forces of soil cohesion and friction, reduced by pore-water pressure of subsurface flow, to destabilizing forces of gravity (Hammond et al., 1992; Wu and Sidle, 1995). The model as given by Pack et al. (1998) is:

$$FS = \frac{(C_r + C_S)/h_s\rho_s g}{\sin\theta} + \frac{\cos\theta \tan\phi(1 - R_w \rho_w/\rho_s)}{\sin\theta} \quad (1a)$$

$$C* = (C_r + C_s)/h_s\rho_s g \quad (1b)$$

C* is a dimensionless cohesion (Eq. 1b) embodying the relative contribution of cohesive forces to slope stability. When C*>1, cohesion is sufficient to hold the soil slab vertically (Pack et al., 1998). *Cr* and *Cs* are root and soil cohesion respectively [Pa], h_s is the soil depth perpendicular to slope [m], ρ_s and ρ_w are saturated soil bulk density and water density [kg/m^3], respectively, *g* is acceleration due to gravity [m/s^2], θ is slope angle of the ground, and ø is soil internal friction angle [°]. Relative wetness, R_w, is defined as the ratio of subsurface flow depth, h_w, flowing parallel to the soil surface, to h_s. Deterministically, a hillslope element is unstable if *FS* < 1 and stable if *FS* > 1 (Sidle and Ochiai, 2006; Shelby, 1993). When FS = 1, the slope is "just-stable" or in a state of "limited equilibrium" (Lu and Godt, 2013).

Relative wetness is arguably the most dynamic factor at short time scales, relating to water table depth and to recharge rate. It is derived from local subsurface lateral flow, q_s [m^2 d^{-1}], represented by a 1-D (i.e., flow parallel to bedrock) form of the kinematic wave approximated by Darcy's law using topographic gradient of hillslope, $q_s = K_s h_w \sin\theta$ (Wu and Sidle, 1995). Under a steady-state assumption, lateral flow is in balance with the rate of water input, q_r [m^2 d^{-1}], through a uniform rate of recharge, R [m d^{-1}], across the upslope specific contributing area, *a* [m], $q_r = Ra$. This assumption gives: $Ra = K_s h_w \sin\theta$, where K_s is saturated hydraulic conductivity [m d^{-1}]. Solving this equation for h_w and dividing both sides by h_s gives R_w (Montgomery and Dietrich, 1994; Pack et al., 1998):

$$R_w = \frac{h_w}{h_s} = \min\left(\frac{R\,a}{T\,\sin\theta}, 1\right) \quad (2)$$

Here *T* is soil transmissivity [m^2 d^{-1}], which is depth-integrated saturated hydraulic conductivity, K_s. For uniform K_s within the soil profile, $T = K_s h_s$. Ground saturates when R_w = 1, which represents hydrostatic conditions and the maximum value for R_w. Options for user-provided *T* or K_s are accepted by the component; although comparison of resulting probabilities were found to be similar given that the value of *T* was derived from h_s. We assume uniform conductivity within the soil profile overlying a relatively impermeable layer such as bedrock,

and subsurface flow direction parallel to this drainage barrier (Montgomery and Dietrich, 1994). These assumptions are appropriate for relatively steep topography and to efficiently characterize wetness over large areas (Tarolli and Tarboton, 2006; van Westen et. al., 2006).

A Monte Carlo simulation is used with equation (1) by assuming R, T, C (C=C_r+C_s), h_s and $\emptyset$ as random variables represented by probability distributions (Tobutt, 1982; Hammond et al., 1992). One benefit of Monte Carlo simulation is that many of the sources of inaccuracy (e.g., nonlinearity, input uncertainties) are overcome (Strenk, 2010; El-Ramly et al., 2002) by generating a distribution of samples over a plausible range for selected variables. The uncertainty in R is defined by using a time series of the maximum daily recharge in each year (e.g., Benda and Dunne, 1997a; Borga et al., 2002; Istanbulluoglu et al., 2004). The model includes both spatially uniform and spatially distributed options for sampling recharge (described further in Sect. 2.3). Using sampled random variables in Eq. (1a), FS is calculated in each model iteration during the simulation. Annual probability of failure P(F) and landslide return period (RP) at each grid cell are defined as (Hammond et al., 1992; Cullen and Frey, 1999):

$$P(F) = P(FS \leq 1) = n(FS \leq 1)/n \quad (3a)$$

$$RP = P(F)^{-1} \quad (3b)$$

Our model does not predict the size of a probable landslide at the initiation point, which can be smaller or larger than the size of a DEM grid. P(F) gives a relative propensity that a landslide could initiate within the grid cell. The design of the model reflects the uncertainty of soil and vegetation within a grid cell. Therefore, if some random samples lead to a low deterministic FS, they contribute to an increase of the P(F) within that cell.

2.2 Model Development in Landlab

The landslide modeling approach presented above is implemented in Landlab (landlab.github.io). Landlab is an open-source modeling toolkit written in Python for building and running two-dimensional numerical models of Earth-surface dynamics (Tucker et al., 2016; Hobley et al., 2017; Adams et al., 2017). A detailed explanation of the Landlab framework is provided in Hobley et al. (2017). Landlab provides a grid architecture, a suite of pre-built components for modeling surface or near-surface processes, and utilities that handle data creation, management, and interoperability among process components. The Landlab design allows for a "plug-and-play" style of model development, where process "components" can be coupled together in a user-customized "model driver". Each component is a set of code functions that represent an individual process; the model driver has code used to import or generate required data, execute the component or set of components used in the model, and to visualize results. For example, once a DEM is imported as a Landlab grid instance, any Landlab component can be used with interoperable methods to attach data and perform operations. Landlab code developed for this work is explained in detail in the user manual of the Landlab LandslideProbability component available from eSurf and the Landlab github website.

Earth Surf. Dynam. Discuss., https://doi.org/10.5194/esurf-2017-39
Manuscript under review for journal Earth Surf. Dynam.
Discussion started: 21 June 2017

The Landlab workflow developed in this regional landslide probability mapping study uses the LandslideProbability component presented in Fig. 1. The workflow includes preparing spatial model parameters and model forcing data completed in preprocessing steps outside of Landlab. A model driver is written to run the LandslideProbability component on RasterModelGrid (RMG) instance only. RMG is a Landlab class for creating raster grids and representing the connections among grid elements. A structured grid is generated that covers the model domain. Spatial model parameters and forcing variables supplied by the user are stored on the grid elements as Landlab data fields, which are NumPy arrays containing data associated with grid elements (in this case nodes). The driver imports Landlab and necessary Python libraries as well as loads and processes data required for the LandslideProbability component.

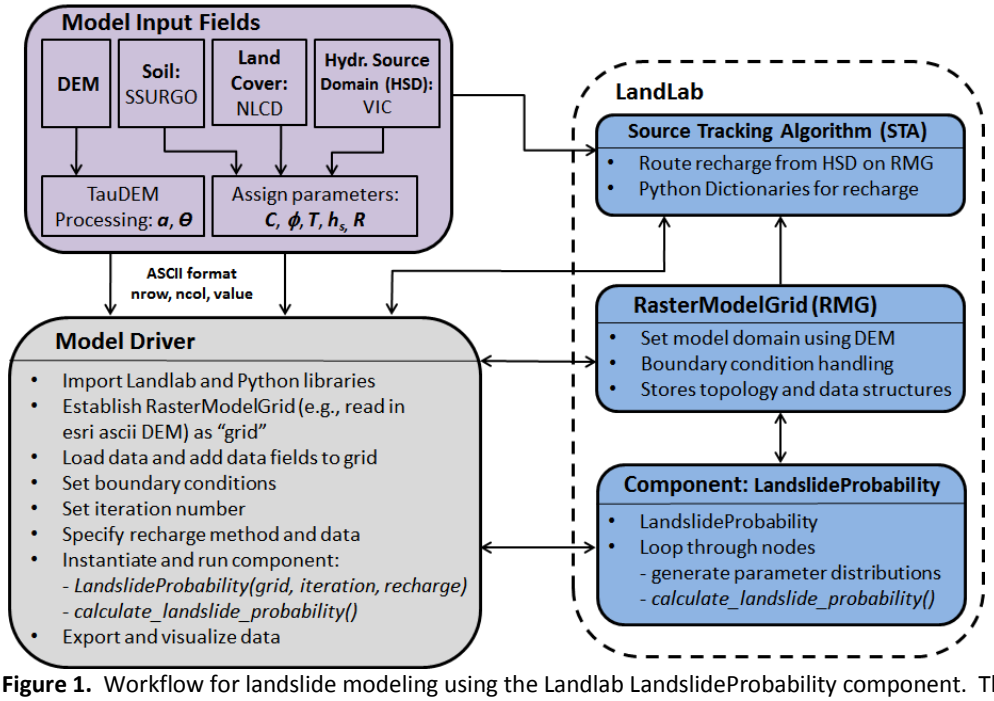

Figure 1. Workflow for landslide modeling using the Landlab LandslideProbability component. The user creates input parameter fields (purple box). The model driver (gray) imports Landlab, Python libraries, and model parameters fields: instantiates (e.g., create an instance) the RasterModelGrid and the component; and runs utilities and methods of Landlab (blue inside dashed box).

Slope angle and specific contributing area are static parameters derived from a DEM in pre-processing steps. Total cohesion, C (i.e., C_r+C_s), ϕ, h_s, and T are treated as random variables following a triangular distribution specified with three parameters (minimum, mode, and maximum) to represent spatial and temporal uncertainties in these parameters on the landscape (Cho, 2007; Dou et al., 2014). Triangular distributions give weight to the most likely value (i.e., mode) and have been proposed in other Monte Carlo simulations of slope stability

(Hammond et al., 1992; El-Ramly et al., 2002; Strenk, 2010). Parameters of the triangular distribution can be assigned by relating categorical vegetation cover variables, for example from the National Land Cover Data (NLCD) (Jin, 2013; USGS, 2014b) or other map sources, with a lookup table for cohesion and using available soils data such as gridded Soil Survey Geographic Database (SSURGO) (*DOA-NRCS* 2016), to assign internal friction angle, soil depth, and transmissivity (see 3.3 for details). Soil density is set as a constant field, 2,000 kg m^{-3} in our application.

In each Monte Carlo iteration, we characterize recharge as an annual maximum daily recharge event. Four options for sampling recharge are provided, which are identified in the model driver by selecting a probability *distribution*: *uniform, lognormal, lognormal_spatial,* and *data_driven_spatial*. The first two assign spatially uniform random variables with respective parameters of minimum and maximum, and mean and standard deviation. The latter two are designed to represent spatial variability in recharge based on historical annual maximum daily recharge routed to each node of the model domain. The *lognormal_spatial* option assigns mean and standard deviation of annual maximum recharge and uses lognormal distribution of recharge for simulation. The *data_driven_spatial* option uses a non-parametric Monte Carlo sampling approach to sample directly from historical recharge data. Upslope-averaged recharge for each grid node is calculated with the Landlab Source Tracking Algorithm (STA) utility using recharge from a HSD, which in this study is the VIC macroscale (1/16° or 5x6 km grid cell) hydrology model.

Within the model driver, the user also sets any boundary conditions, such as areas to exclude (i.e., bedrock outcrops, glaciers) and assigning the number of Monte Carlo iterations (n>>1,000, Hammond et al., 1992). The LandslideProbability component is instantiated by passing four arguments: the grid, number of iterations, recharge distribution, and recharge parameters. Multiple instances of the LandslideProbability class can be established in one driver to compare the results from different recharge specifications. Once the component has been instantiated, the component's method *calculate_landslide_probability()* is run. For each iteration, this method loops through each core node, generates unique model parameters, and calculates the relative wetness (Eq. 2) and deterministic FS index (Eq. 1a) at each iteration. At the end of the iterations, the P(F) at the node is calculated as the number of iterations in which FS≤1 divided by the number of iterations. Variables output by the component at each core node include calculated probability of saturation and P(F), which can be queried at each node or visualized across the entire grid within the driver or using a command line terminal to execute commands.

2.3 Hydrologic Data Processing

A key aspect of the regional landslide modeling approach is the linking of landslide hazard to hydro-climatological forcing at regional scales. The Landlab LandslideProbabilty component is written with the capability to accept input from hydrologic model outputs. We used the VIC macroscale hydrologic model (Liang et al., 1994) to demonstrate this capability because it characterizes elevation-dependent differences in regional precipitation and temperature forcings and their influence on recharge through regulating snow accumulation and melt, rain-

on-snow, evapotranspiration, and soil moisture. VIC is semi-distributed, predominantly physics-based macro-scale hydrology model, which is advantageous for representing distributed parameters of hydro-climatology that are not stationary in time over large regional areas (Hamlet et al., 2013).

The VIC model simulates the land surface as a large, flat, uniform grid with sub-grid heterogeneity (e.g., vegetation and elevation) based on statistical distributions. Daily or sub-daily meteorological drivers (e.g., temperature and precipitation) influence the fluxes of water and energy near the land surface. Each grid is simulated independently and flows between grid cells are ignored (e.g., unrouted). Precipitation enters the upper of typically three layers of soil and infiltrates to lower layers via a variable infiltration curve. Soil water can move between layers vertically and is lost through evapotranspiration and from the third layer as base/subsurface flow via non-linear recession. Water input in excess of infiltration forms surface runoff.

To characterize the annual probability when the ground is likely to be the most saturated, daily baseflow and surface runoff are summed at each VIC grid cell to represent recharge [mm d^{-1}] and the annual maximum daily value is selected for each model year, similar to others (e.g., Benda and Dunne, 1997a; Borga et al., 2002; Istanbulluoglu et al., 2004). The recharge data arrays are keyed to latitude, longitude, and grid cell ID (a user-defined ID for each VIC grid cell, in our case) packaged as Python dictionaries (see Fig 1. of User Manual). To help account for lateral fluxes in groundwater (van Beek, 2002), VIC recharge is routed to each node in the model grid using the STA utility, which also addresses the different spatial resolutions of VIC and the RMG. This Landlab utility was developed to derive the fraction of annual maximum recharge from each VIC grid cell within the upslope contributing area of each Landlab grid node. The fractions and VIC IDs are saved as values for two Python dictionaries keyed to the RMG node ID. At each node, these dictionaries are used to calculate the upstream proportionally-averaged maximum recharge for each year.

2.4 Soil Depth Evolution Model

Soil depth controls the temporal and spatial patterns of landsliding over geomorphic time scales and is considered one of the most significant parameters controlling the FS stability index, especially at depths less than 1.5 m (Benda and Dunne, 1997a; Istanbulluoglu et al., 2004; Catani et al., 2010; Sidle and Ochiai, 2006). Soil depth can vary in space and time as a function of weathering and sediment transport in relation to climate, lithology, topographic position, and vegetation cover (Dietrich et al., 1995). As an alternative to spatial soil maps such as the SSURGO database (*DOA-NRCS* 2016), which are often produced at the soil pedon-level, we developed a soil depth map using a simple soil evolution model and topographic and land cover attributes (Dietrich et al., 1995; Pelletier and Rasmussen, 2009; Tesfa et al., 2009; Bellugi et al., 2015).

Earth Surf. Dynam. Discuss., https://doi.org/10.5194/esurf-2017-39
Manuscript under review for journal Earth Surf. Dynam.
Discussion started: 21 June 2017

Change in soil depth depends on soil production by bedrock weathering and slope-dependent sediment transport expressed as (Nicótina et al., 2011; Tucker and Slingerland, 1997; Heimsath et al., 1997):

$$\rho_s \frac{\partial h_s}{\partial t} = -\rho_r \frac{\partial z_b}{\partial t} - \rho_s \nabla q_s \quad (4)$$

where ρ_s and ρ_r are bulk densities for soil and rock, respectively, h_s is soil depth, z_b is the elevation of the soil-bedrock interface, t is time, ∇ is the topographic divergence operator for the topographic gradient, and q_s is the sediment flux. The soil production rate (e.g., first term in Eq. 4 on right side) is a function of the rate of change in the elevation of the soil-bedrock interface, which has been shown to decline exponentially with soil depth (Heimsath et al., 1997, Gabet et al., 2003):

$$\frac{\partial z_b}{\partial t} = -P_o e^{-\alpha h_s} \quad (5)$$

where P_o is the soil production rate from exposed bedrock (i.e., no soil cover) and α is the rate of exponential decay with depth. Diffusive sediment transport characterized in the second term on the right side of Eq. (4) can be represented by a simple soil creep function dominant in convex hillslopes as (Nicótina et al., 2011; Istanbulluoglu et al., 2004):

$$\nabla q_s = -K_d \nabla^2 z \quad (6)$$

where K_d is a linear hillslope diffusion coefficient and ∇^2 is Laplacian of elevation. Dividing Eq. (4) by ρ_r, multiplying by the ratio of ρ_r / ρ_s, and substituting Eq. (5) and Eq. (6) into Eq. (4), yields the following instantaneous soil depth equation:

$$\frac{\partial h_s}{\partial t} = \frac{\rho_r}{\rho_s} P_o e^{-\alpha h_s} + K_d \nabla^2 z \quad (7)$$

The change in soil depth with time based on Eq. (7) is added to the soil depth at *t-1* (*t* in years) to evolve soil depth over time (see also: Pelletier and Rasmussen 2009).

Variable curvature profiles, steep and planar hillslopes, and abrupt knife edge drainage divides indicate nonlinear transport processes such as mass wasting (Roering et al., 2004, 1999). These landscape characteristics are common in the steep terrain; therefore, in every iteration of the model Eq. (a) and Eq. (2) are used to calculate FS within the soil evolution model. When FS≤1, soil is removed to bedrock by setting it to a very small value of 0.005 m to be consistent with the creep equation. In each model iteration, C and T, were randomly sampled and used deterministically in the FS Eq. (1a). Calibration of the soil evolution model is done by adjusting P_o and K_d for the location of the landslide analysis based on published long-term rates of erosion and diffusion. Creation, calibration, and application of the soil evolution model are detailed in Sect. 4.1.2.

2.5 Reproducibility

To publish a reproducible version of this research, we used the HydroShare (www.hydroshare.org) cyberinfrastructure platform, which is designed explicitly to encourage the reusing and sharing of models (Tarboton et al., 2014; Horsburgh et al., 2016; Morsy et al., 2017). Steps that supported reproducibility included using the HydroShare sharing settings

Earth Surf. Dynam. Discuss., https://doi.org/10.5194/esurf-2017-39
Manuscript under review for journal Earth Surf. Dynam.
Discussion started: 21 June 2017

with a workflow that started with *Private* while data and models were developed, *Discoverable* while research was being shared with colleagues for review, and *Public*, once our results were accepted for publication. We used the *Select a license* function to add No Commercial (NC) use to our Creative Commons license. We made use of the *Groups* social collaboration, by making early versions of our research results available to invited participants of workshops and tutorial demonstrations to our Landlab group in HydroShare. The data and model are accessed by launching Jupyter Notebooks that access Landlab installed on JupyterHub servers at the National Center for Supercomputing Applications (Yin et al, 2017; Castranova, 2017). HydroShare features enable our current and future researchers to use the *Copy Resource* function to replicate our published resource (i.e., the landslide model) in their own account with *Derived from* metadata that references back to the published resource DOI, to serve as a starting point for their work.

3 Model application

3.1 Study Area

The model described above is applied within the geographical limits of the North Cascades National Park Complex (NOCA) in the state of Washington, U.S.A, managed by the U.S. National Park Service (Fig. 2). In recent decades, NOCA has experienced damaging and disruptive landslides that have impacted infrastructure and the public. Furthermore, the park area is covered by a recent soil survey between 2003 and 2009, including field investigation (DOA-NRCS and DOI-NPS, 2012), and has a complete map of mass wasting processes visually observed in the field (Riedel and Probala, 2005).

NOCA is approximately 2,757 km^2, with 93% wilderness (in which no motorized or mechanized devices are permitted; DOI-NPS, 2012), which is ideal for studying naturally triggered landslides. The elevation ranges from about 100 m to 2,800 m (Fig. 2a). The terrain is composed of rock slopes at the highest elevations, short (<100 m) soil-mantled hillslopes, and landslides upslope of relatively straight debris flow channels connected to the fluvial system. Over 300 glaciers occupy mountain peaks in NOCA. The influence of the Pacific Ocean, approximately 80 km to the west, provides a humid temperate climate. However, the north-south oriented Cascade Mountains create an effective orographic climate boundary, separating a wetter west side from a drier east side. Reported mean annual precipitation ranges from about 708 mm in the low elevations of the eastern slopes to 4,575 mm at the highest mountain elevations west of the Cascade crest, with about 70% falling in November through March (Fig. 2b). This spatial precipitation gradient is the result of orographically-enhanced precipitation that leads to a strong rain shadow (Roe 2005). Average annual air temperatures range from -2 to 11°C, depending on elevation (DOA-NRCS and DOI-NPS, 2012).

Vegetation is mainly coniferous trees, with deciduous trees along river floodplains, and shrubs, meadows, and barren land in the subalpine and alpine environments. In this study vegetation classes were grouped into herbaceous, shrubland, and forest using the 2014 NLCD data, which is based on the land use/land cover (LULC) classification of 2011 Landsat satellite imagery (Jin,

2013; USGS, 2014b). Based on this classification, forest, shrubs, and herbaceous vegetation represent 58%, 17%, and 12% of the park, respectively. Elevation ranges for these vegetation classes are from 106 to 2363 m (forest), 110 to 2465 m (shrubs), and 121 to 2759 m (herbaceous).

The park geology is composed of a complex mosaic that includes mostly complexly faulted and folded sedimentary and volcanic rocks on the west side, unmetamorphosed sedimentary and volcanic rock on the eastern edge, and highly squeezed and recrystallized metamorphic rock originating from great depth in middle (Haugerud and Tabor, 2009). Alpine and continental glaciation, along with rivers and mass-wasting processes, have created the landscape we observe today. The glaciers eroded U-shaped valleys with steep valley walls prone to landslides and flat valley floors with gravel-bed rivers. The lower ends of many valleys on the east side were not covered in alpine glaciers and have narrow, winding V-shaped canyons and steep, narrow rivers.

A park-wide landform mapping study identified six different types of mass wasting: rock fall/topple, debris avalanche, debris torrent, slump/creep, sackung, and snow avalanche-impacted landforms (Riedel et al., 2015). Mass wasting landforms were identified in the landform mapping using 1998 air photos at 1:12,000 scale, 7.5 minute topographic maps, bedrock geology maps, and field investigations. The minimum mapping unit was approximately 1,000 m^2, except for a few smaller slump units. In this study, we only used mapped debris avalanches for model confirmation as they often initiate by shallow landslide processes. Debris avalanches typically represent a mixture of failed rock and debris and the mapped polygon included head scar, transport and scour channels, and deposition zone represented in a single polygon (Fig 3a). We extract the highest 10% of the elevations in the mapped debris avalanche polygons as landslide source areas through comparison to aerial imagery (Tarolli and Tarboton, 2006). Landslide sources are more frequent in the intermediate elevations. In the NOCA region, 75% of landslide source areas are located in the 1,200 m to 2,000 m elevation range (Fig. 3b).

Earth Surf. Dynam. Discuss., https://doi.org/10.5194/esurf-2017-39
Manuscript under review for journal Earth Surf. Dynam.
Discussion started: 21 June 2017

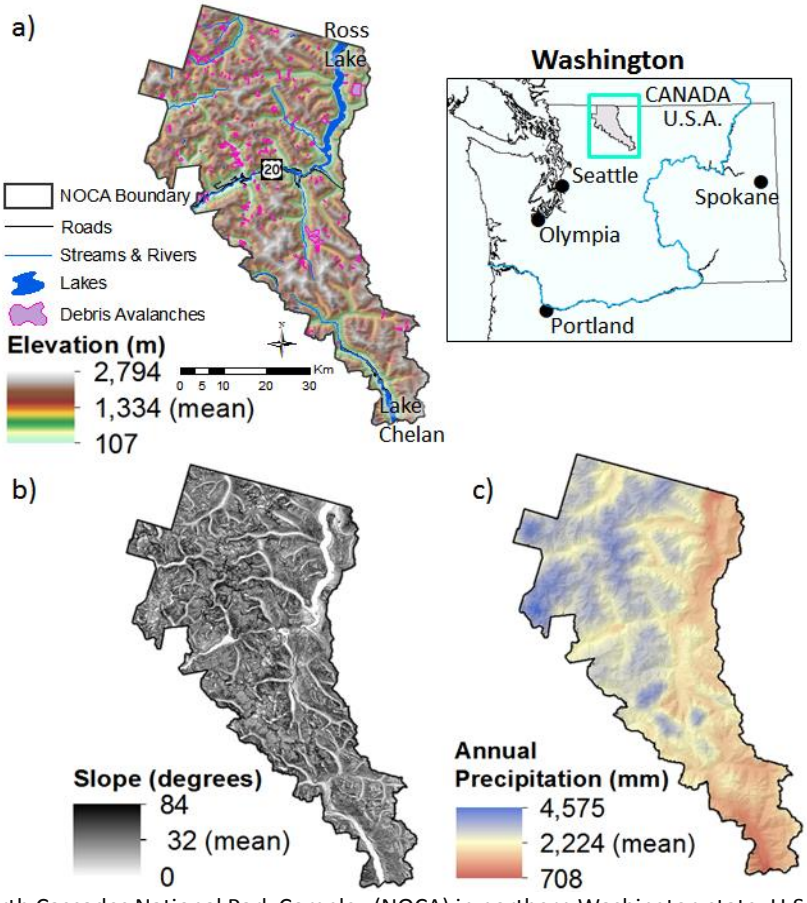

Figure 2. North Cascades National Park Complex (NOCA) in northern Washington state, U.S.A: **(a)** a 30-m DEM of the domain overlain by debris avalanches and major water bodies; **(b)** slope derived from DEM; and **(c)** mean annual precipitation (1981-2010 average) mapped at 800-m resolution from PRISM (PRISM Climate Group, 2004).

Some areas in mountainous regions are covered by glaciers, permanent snowfields, and exposed bedrock, which are unsuitable locations to model landslides on soil-mantled hillslopes using the infinite slope model (Borga et al., 2002). Furthermore, they are not expected to be destabilized by precipitation, although other forces could cause failures (e.g., earthquake, volcanic activity, and temperature). We exclude high elevation areas covered by glaciers, permanent snowfields and exposed bedrock (Fig 3c), as well as wetlands and other water surfaces, based on landform mapping and maps of lithology and LULC, from our modeling domain and geomorphic analysis because shallow landslides are not typically observed on these landforms. The total area excluded from the stability analysis accounts for about 21% of NOCA's land area.

Earth Surf. Dynam. Discuss., https://doi.org/10.5194/esurf-2017-39
Manuscript under review for journal Earth Surf. Dynam.
Discussion started: 21 June 2017

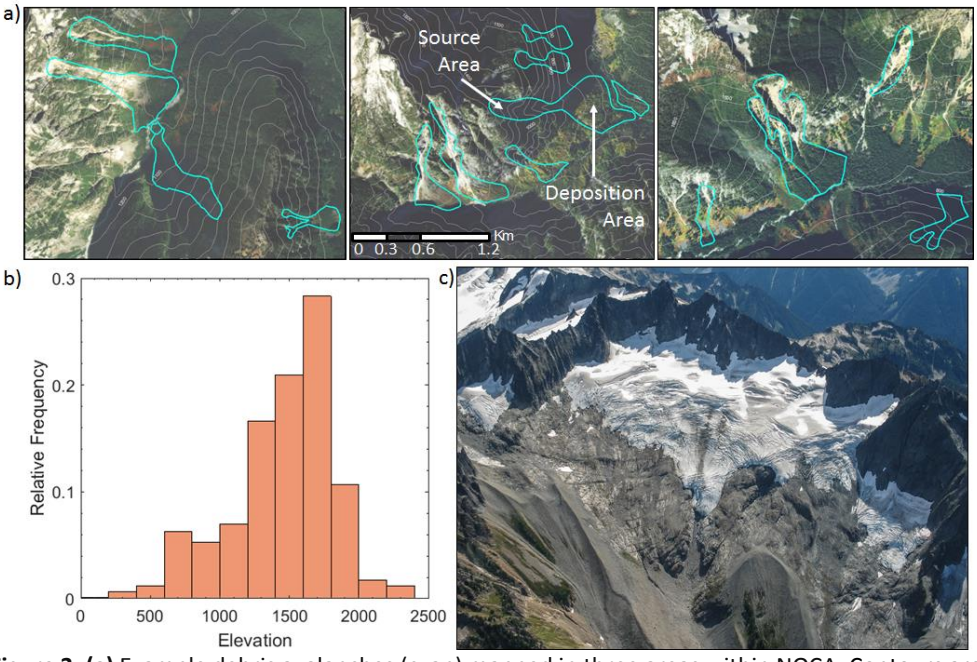

Figure 3. (a) Example debris avalanches (cyan) mapped in three areas within NOCA. Contours are in 100-m intervals. Aerial image source from World Imagery, Esri Inc.[1]; **(b)** elevation distribution of the relative frequency of mapped debris avalanche source areas (upper 10%); and **(c)** High elevation rock and glacier mapped surrounding Spiral Glacier in North Cascades showing a bedrock glacier cirque with thin barren soils and moraine deposits (photo by John Scurlock with permission).

3.2 Model Input Fields

We used a grid resolution of 30 m to evaluate and compare our regional model of landslide probability to a limited set of landslide observations. A 30-m grid cell size is consistent with the minimum mapping unit used for landslides (Riedel et al., 2015; see also Regmi et al., 2014). Slope ($S=\tan\theta$), combined curvature (Curv), and contributing area (CA) attributes were derived from a 30-m DEM acquired from *National Elevation Dataset* (NED) (USGS, 2014a) (Fig. 2a). In addition, the NLCD data for vegetation classification and the SSURGO soils database we used in this study both have available 30-m grid resolutions. To show the model potential for regional applications, a global coverage of 30-m DEM from the NASA Shuttle Radar Topography Mission (SRTM) is available (USGS 2017). Thus, showing the model's potential at this resolution is intended in this paper, especially for regional applications beyond the use in a single watershed across the globe.

[1] Images created using ArcGIS® software by Esri. ArcGIS® and ArcMap™ are the intellectual property of Esri and are used herein under license. Copyright © Esri. All rights reserved. For more information about Esri® software, please visit www.esri.com.

Earth Surf. Dynam. Discuss., https://doi.org/10.5194/esurf-2017-39
Manuscript under review for journal Earth Surf. Dynam.
Discussion started: 21 June 2017

3.2.1. Vegetation and Soil parameters

Parameters of a triangular distribution for *C, ø, T, and* h_s are provided in Table 1. In our case study, *C* represents root cohesion because we assumed soils to be primarily cohesionless, due to low clay content in this mountain substrate. We developed spatial coverages for minimum, mode, and maximum C for NOCA by relating vegetation classes with corresponding published C values in the literature (Table 1), where field observations suggest right-skewed distribution (Hammond et al., 1992; Schmidt et al., 2001; Gabet and Dunne 2002; Hales et al. 2013). Based on ranges available in the literature, we selected a mode value as a commonly reported value, minimum parameter as 30% of the mode, representing death and loss of productivity (Sidle, 1991; 1992), and a maximum near the highest reported value for C. Other LULC types include water, wetland, snow/ice, barren, and developed (e.g., roads, campground). Small C values are assigned for barren and developed land uses (~14% of the domain) having minimal vegetation. Mode values of C mapped over NOCA are given in Fig. 4b.

Table 1. Parameters defined for vegetation and soil types in the study region. For spatially continuous parameters, values represent the statistics for the model domain with *(mean)* values in parentheses.

Parameter	Minimum	Mode *(Mean)*	Maximum
Root Cohesion [kPa]			
Barren/Developed	0.03	0.10	0.15
Forest (coniferous)	3	10	20
Shrubland	1.2	4	10
Herbaceous	0.6	2	5
Internal angle of friction [°][1]			
Loamy sand	26.2	32	42.2
Sandy loam	28.7	35	46.2
Developed areas (loamy, sandy)	28.7, 31.2	35, 38	46.2, 50.2
Transmissivity [m^2 d^{-1}][2]	0.42	*(3.39)*	16.4
Soil depth [m][†]	0.09	*(0.62)*	2.01

[1] Developed areas within the two soil types, respectively, have mode values 3° larger due to compaction.
[2] Values for the continuous variables, transmissivity and soil depth, represent the minimum, mean, and maximum for the study area, not individual soil map units.

Despite the aggregation of plant types into functional plant communities (Fig. 4a), considerable spatial variability in C is present within the park (Fig. 4b), with the greatest values in the forest communities of the valley bottom and lower valley walls. As communities transition from forest to shrublands to herbaceous species with increasing elevation, C declines. Note that herbaceous species are likely composed of considerable woody vegetation in this alpine region, but of diminutive stature.

In order to investigate the contribution of soil depth to mapping landslide probability, we developed and used two alternative soil depth products. The nationally available SSURGO

database maintained by the Natural Resources Conservation Service (NRCS) is a readily available data source that includes depth-to-restrictive layer (*DOA-NRCS* 2016), which we used to specify the mode of soil depth (Fig. 4c). Using the *Soil Data Viewer* of Esri ArcGIS (DOA-NRCS, 2015a), the weighted-average aggregation option is used to extract soil depth within each soil map unit (DOA-NRCS and DOI-NPS, 2012). SSURGO soil depth (SSURGO-SD) is uniform for each soil map unit and thus, lacks finer scale spatial heterogeneity and create edge incongruities (Fig. 4c), a limitation also identified in other landslide modeling studies (Bordoni et al., 2015). A smoother and spatially consistent soil depth map is achieved using the soil evolution model.

SSURGO-SD represents the recent conditions in soil depth. The difference between the actual soil depth in the field and the SSURGO reported soil depth will likely be associated with the limited number of soil depth measurements used to develop SSURGO maps, measurement errors, and spatial interpolation assumptions. In addition, for the locations that have already produced landslides before SSURGO mapping, we assume that the maximum value of the triangular distribution represents the soil depth prior to a landslide. To represent uncertainty, minimum h_s is assumed to be 70% of the mode and maximum h_s adds 10% to the mode value. These values give a left-skewed triangular distribution, commonly used in probabilistic landslide models (Hammond et. al., 1992). Selected ranges were confirmed by the soil evolution model discussed in Sect. 4.1.2.

Transmissivity is derived as the product of weighted-average aggregated K_s of all soil layers above the restrictive layer and h_s for each soil map unit (DOA-NRCS, 2015a). Similar to h_s, this T value was considered the mode (Fig. 4d) and the minimum and maximum values needed for an asymmetrical triangular distribution calculated as: $T_{min} = T_{mode} - 0.3*T_{mode}$ and $T_{max} = T_{mode} + 0.1*T_{mode}$. Closely related to soil depth, transmissivity is high in valley bottoms as well on plateaus because of deeper soils, thus, more water can move through the soil when saturated (Fig. 4d). Transmissivity is low in the thin veneer soils below retreating glaciers as well on steeper side slopes.

Soil surface texture is a grouping used to describe the particle size distribution of granular media, and can be used as an indicator of ø (Nimmo, 2005). The percent sand, silt, and clay (weighted-average aggregation) for each soil map unit in NOCA were derived from SSURGO data using Soil Data Viewer (DOA-NRCS, 2015b). This revealed largely sandy loam or loamy sand soil textures, based on USDA classification, across the NOCA. These soil textures corresponded to Unified Soil Classification System (USCS) soil types silty sand and well-graded (diverse particle size) fine to coarse sand, respectively. Reported ø values for these USCS soil types were assigned as the $ø_{mode}$ (i.e., Table 5.5 in Hammond et al., 1992 and Table 5.2 in Shelby, 1993). Developed land cover type was assigned an additional 3° to the mode to compensate for higher soil density from development activity, such as compaction (Sidle and Ochiai, 2006). The map of ø exhibits the least variability in NOCA due to the relatively narrow range of soil textures, with lower angles typical at higher elevation and higher angles farther downslope (figure not shown). Given the mode and ranges of ø for these soil types, minimum and maximum ø were calculated to generate right-skewed distributions for both soil types as: $ø_{min} = ø_{mode} - 0.18*ø_{mode}$

Earth Surf. Dynam. Discuss., https://doi.org/10.5194/esurf-2017-39
Manuscript under review for journal Earth Surf. Dynam.
Discussion started: 21 June 2017

and $ø_{max} = ø_{mode} + 0.32*ø_{mode}$. The soil and water density terms in Eq. (1a), were assigned a constant value of 2,000 kg m^{-3} and 1,000 kg m^{-3}, respectively (Pack et al., 2005).

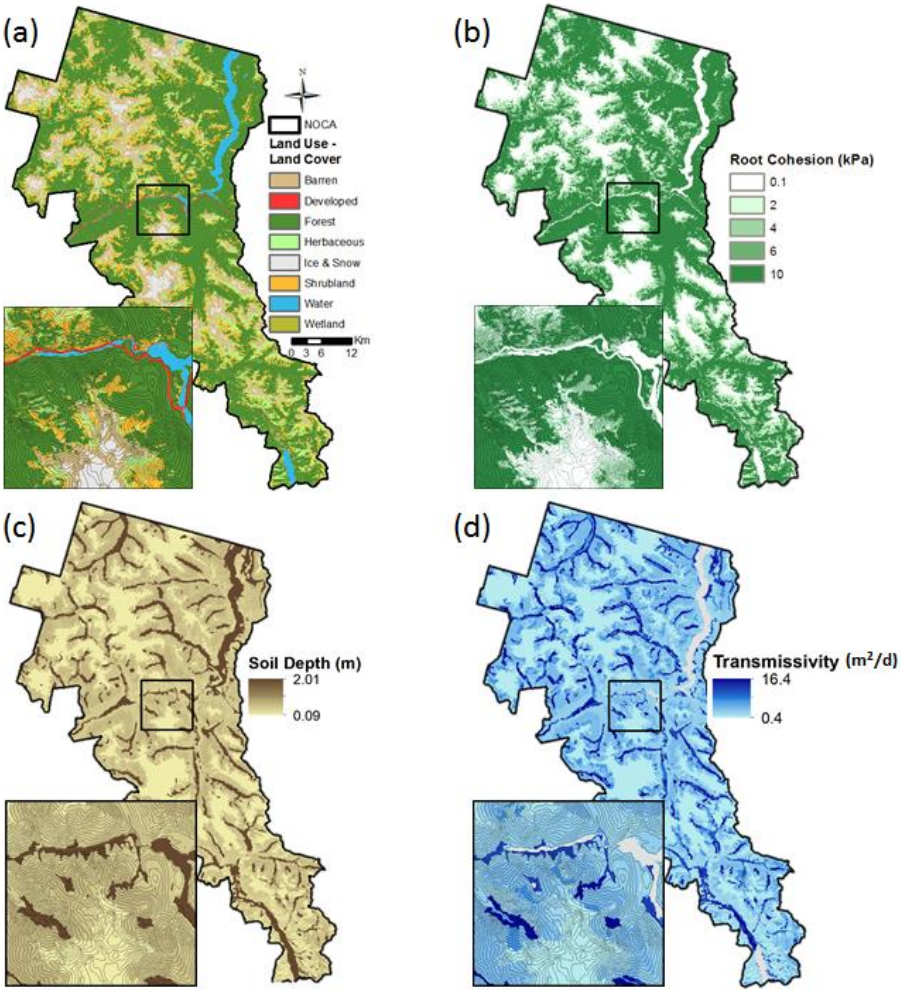

Figure 4. Distributed parameters used in the landslide model over NOCA, including: **(a)** LULC classified from NLCD (2014); **(b)** root cohesion based on LULC; **(c)** soil depth from SSURGO; and **(d)** transmissivity based on SSURGO soil depth. Mapped values in (b) through (d) represent the mode values used in the parameter distributions. Insert shows zoomed-in area with 100 m contours.

Earth Surf. Dynam. Discuss., https://doi.org/10.5194/esurf-2017-39
Manuscript under review for journal Earth Surf. Dynam.
Discussion started: 21 June 2017

3.2.2. Model Recharge

The model is designed with a flexible approach to parameterizing recharge. Available probability distributions include uniform, lognormal, lognormal spatial, and data driven spatial. Supplemental materials include a Jupyter Notebook that reproduces these four recharge options on a synthetic grid. To provide the hydro-climatology forcing to drive our landslide model, our model application leverages the existing detailed simulations of VIC in the PNW region developed through the *Columbia Basin Climate Change Scenarios Project* (Elsner et al., 2010; Hamlet et al., 2013). The project developed a calibrated implementation of VIC (1/16° or 5x7 km grid resolution) covering the Columbia River basin in Washington to produce validated historical hydrologic simulations (water years 1916-2006) driven by spatially interpolated daily station observations of temperature and precipitation (Hamlet et al., 2013). Archived model output at a daily-time-step includes gridded baseflow and runoff. Hydrologic simulations using VIC have also been run for all of the contiguous United States (CONUS; Livneh et al., 2013, 2015). Thus, acquisition of hydrologic model output is readily available to apply the landslide model anywhere throughout the CONUS. We determined the maximum daily recharge for each year to generate a 91-year long time series to calculate the annual highest pore-water pressure at each VIC grid cell. Modeling with maximum recharge provides an indicator of individual storm events that typically trigger shallow landslides (Lu and Godt, 2013), although lesser amounts of recharge may also be sufficient to trigger landslides in some locations.

4 Results and Discussion

4.1. Geomorphic Analysis and Soil Evolution

Understanding the spatial distribution of dominant geomorphic processes can aid the development of landslide hazard maps consistent with geomorphic theory. In this section, we discuss the mapping of dominant processes on the landscape on the slope and area domain, and explore the proposed soil evolution model to develop modeled soil depth maps.

4.1.1. Investigation of Process Domains

Hillslope diffusion, landslide, debris flow, and fluvial transport processes leave unique imprints on landforms, manifested in the slope-contributing area (S-CA) domain as different scaling relationships (Montgomery and Dietrich, 1992; Tucker and Bras, 1998; Montgomery, 2001; Stock and Dietrich, 2003; Tarolli and Fontana, 2009). The infinite-slope factor-of-safety model is only applicable to the initiation of landslides. Therefore, hazards associated with debris flow scour and deposition cannot be predicted by this model. We used a S-CA plot and the infinite slope stability theory to: (1) identify process domains and limit the analysis of the landscape to slopes where there is shallow landslide potential, (2) evaluate observations of debris avalanches to identify landslide source areas, and (3) infer plausible ranges of the infinite slope stability model parameters to corroborate those we compiled from the literature for NOCA (Table 1).

Earth Surf. Dynam. Discuss., https://doi.org/10.5194/esurf-2017-39
Manuscript under review for journal Earth Surf. Dynam.
Discussion started: 21 June 2017

Our geomorphic analysis was based on plotting, in log-log scale, S, (=tan(θ), and CA pairs of each DEM grid cell in NOCA, cells within mapped debris avalanches (including depositional areas), and most likely source areas of landslides identified as the single highest elevation grid cell within each mapped debris avalanche (Fig. 5). The general trend in the S-CA relationship is acquired for all grid cells of NOCA as well as debris avalanche (DA) cells by binning the data with respect to CA and calculating the mean S for each CA bin. The negative linear relation in the log-log plot suggest a power-law scaling in the form of $S \sim CA^{-B}$ where B is the slope of the S-CA relation on the log-log domain, which reflects channel longitudinal profile concavity. Concavity is generally associated with the role of discharge (CA is used as a surrogate in this plot) in enhancing sediment transport, while the degree of concavity is tightly related to how nonlinear the dominant transport is with respect to S and CA (Roering et al, 1999; Montgomery 2001; Istanbulluoglu 2009). Geomorphic process domains interpreted from the binned S-CA plot portrayed in Fig. 5 include: (1) a hillslope zone where slope-dependent processes such as dry ravel and soil creep dominate, leading to convex slopes, (2) a landsliding zone where pore-pressure driven slope failures introduce concavity as landslides arise with shallower slopes as recharge CA grows, (3) a debris flow or saturated landslide zone in headwater channels where mass wasting processes are supplemented with higher fluidity and ground saturation leading to S and CA driven high-concentration transport (Iverson et al., 1997), and (4) a fluvial region where stream-dominated erosion and transport processes ensue (Montgomery and Foufoula-Georgiou, 1993; Tucker and Bras, 1998). Dominant process domains in the S-CA plot are identified by visual inspection of the scaling transitions that mark changes in concavity. It is well documented that debris flows show reduced concavity relative to both channels and pore-pressure driven landslide zones in the S-CA domain (Montgomery and Foufoula-Georgiou, 1993; Tucker and Bras, 1998; Stock and Dietrich, 2003). The highest profile concavity results from fluvial transport (Fig. 5).

Earth Surf. Dynam. Discuss., https://doi.org/10.5194/esurf-2017-39
Manuscript under review for journal Earth Surf. Dynam.
Discussion started: 21 June 2017

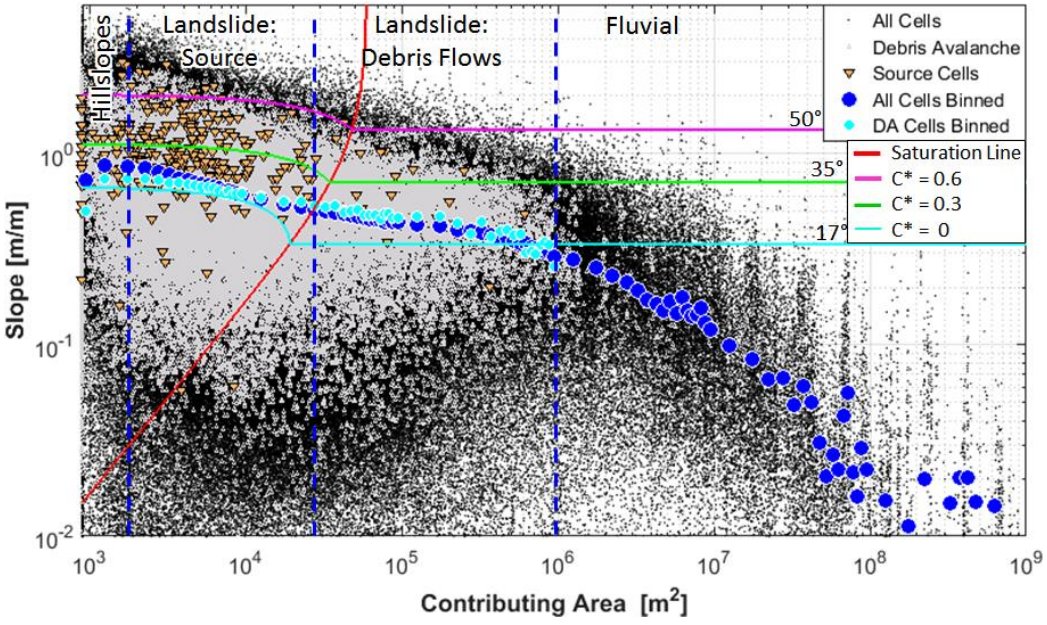

Figure 5. Slope-contributing area (S-CA) plot for North Cascades National Park Complex. Mean S for bins of CA are indicated by blue dots and cyan dots for all cells and debris avalanche (DA) cells, respectively. DA source cells (orange triangles) are the single highest elevation grid cell within mapped debris avalanches (gray). Slope stability curves plot the solution of Eq. (1a) for FS=1, given C* and ø=34°. Above each curve landscape is unstable for a given C*. Saturation line (red curve) separates partially saturated areas (left) from saturated areas (right). Vertical lines divide the plot into geomorphic process domains in relation to CA of the landscape (e.g., Montgomery 2001). Cyan horizontal line at 17° generally separates potential landslide dominated areas from fluvial dominated areas.

A threshold CA of approximately 1 km^2 and a slope threshold of θ=17° generally separates colluvial mass wasting and debris transport processes from fluvial processes (Fig. 5; see also Legg et al., 2014). Nearly all grid cells within mapped debris avalanches plot to the left of the 1 km^2 dashed line. An average θ value of 17° may also correspond to a low-end of a slope threshold for landsliding. Fully saturated cohesionless soils are unconditionally stable at tan(θ) ≤ ½ tan(ø) (i.e. half of ø), assuming a ratio of water to saturated soil density of 0.5 (e.g., Montgomery and Dietrich, 1994). Solving for ø when θ = 17° gives 34°, generally consistent with selected ø values from soil texture (Table 1) (Hammond et al., 1992). Approximately 85% of NOCA landscape lies above θ > 17°, suggesting a dominant role of mass wasting processes in this landscape. We included areas above this slope threshold in our landslide model domain.

The red saturation curve is calculated as aR/T, where R/T is calibrated to 0.0005 m^{-1} (e.g., $a/sin\theta$ = 2000 m) to capture most of landslide source cells (left of curve) and a scaling break in the binned S-CA plot (Fig. 5). The saturation curve partitions the landscape into partially saturated (left) and saturated (right) areas, which generally delineates the S-CA pairs separating landsliding from debris flow tracks that form under full soil saturation. For a T = 10 m^2 d^{-1}, R is 5

mm d^{-1}, which is within the range of the lowest maximum annual modeled recharge values in most of the study area, indicating that the plotted saturation line could reasonably map regions that experience saturation annually.

The three lines stacked vertically plot the solution of S in the infinite slope stability equation (Eq. 1a and 2) as a function of CA, and given FS=1, R/T=0.0005, ø=34° and select values of dimensionless cohesion, C*. Conditioned on the C* value, slopes that plot above the S-CA solution are unstable. Consistent with the binned S-CA data, the solution of the infinite slope stability equation curves down as a function of CA, and following soil saturation, a constant instability S threshold is reached. Root cohesion is approximately 6 kPa for C*=0.3 (middle green line) and 12 kPa for C*=0.6 (upper pink line), assuming a soil depth of 1 m. These root cohesion values are reasonable for shrub and mature forest vegetation found in the literature (Table 1) and they facilitate stability with steeper slopes. When C*=0 (bottom cyan line), landslides initiate at lower slopes than when cohesion is greater. This solution also envelops the low slope-end of nearly all landslide source S-CA pairs identified from debris avalanche data. Only a small portion of the unstable areas plot above the C*=0.6 solution of Eq. (1a), which implies areas with higher root cohesion.

4.1.2. Evolved Soil Depth

We ran the soil evolution model described in Sect. 2.4 at representative topographic conditions and used the results in a nonlinear regression analysis to estimate soil depth from slope and total curvature. As the study domain is large, we used a representative population of θ [^{o}], CA, and Curv values to run the soil evolution model for different vegetation types. The resulting nonlinear equations were used to estimate the mode of modeled soil depth (M-SD) of each vegetated grid cell of the study domain. Capitalizing on the S-CA analysis (see Sect. 4.1.1), θ, CA, and Curv triplets in each of the CA bins are used from the landscape dominated by colluvial transport processes (θ>17^o and CA≤1 km^2). In order to further classify landscapes within each CA bin, θ and Curv pairs are grouped into shallow ($\theta \leq$ the 10th percentile θ), moderately steep (between 10th and 90th percentiles of θ), and steep ($\theta \geq$ the 90th percentile θ) slope classes. Within each class, θ and Curv are averaged.

We ran the soil evolution model for 10,000 years to represent the postglacial landscape (i.e., roughly the current interglacial period or Holocene) using the calibrated parameters listed in Table 2, allowing soil sediments to develop from bedrock and to be removed through diffusive and mass wasting processes. We ran the soil model for the three slope classes and for mature forest, shrubs, and herbaceous root cohesion (Table 1). Mean and mode soil depth were calculated for a given θ, CA, and Curv for each vegetation type.

Earth Surf. Dynam. Discuss., https://doi.org/10.5194/esurf-2017-39
Manuscript under review for journal Earth Surf. Dynam.
Discussion started: 21 June 2017

Table 2. Model parameters used in the soil evolution model

Parameter	Value	Units
h(initial) – initial soil depth	0.01	m
α – rate of exponential decay with depth	3	m^{-1}
Po – soil production rate from exposed bedrock	0.0005	m yr^{-1}
Kd – linear hillslope diffusion coefficient	0.01	m^2 yr^{-1}
ρ_r / ρ_s – Rock to soil density density	2.65/2	[-]
Ks – saturated hydraulic conductivity	7	m d^{-1}
ø – internal angle of friction	35	Degrees
Root cohesion[1]	Varies	kPa
Recharge (mean)[2] and Coefficient of variation	32, 0.35	mm d^{-1}

[1] Root cohesion varied by vegetation type based on Table 1 and soil cohesion was assumed to be zero.
[2] Recharge extracted from average values found at four representative VIC grid cells within NOCA.

Both θ and Curv have been found to be correlated with soil depth (Heimsath et al., 1997; Braun et al., 2001; Mitchell and Montgomery, 2006; Hren et al., 2007). A multivariate nonlinear regression in the form of $y=\beta_1 \cdot x_1^m+\beta_2 \cdot x_2+C$ was fit to mean and mode of soil depth (predictand, y) given θ and Curv (predictors, x_1 and x_2) for each vegetation type with R^2 >0.9 for all slope classes (not reported). Maps for mode of the modeled soil depth (M-SD) were developed over the portion of the NOCA domain by applying the regression equations using the distributed θ and Curv appropriate for vegetation type at each grid cell. Minimum and maximum depth were set at 0.005 and 2 m, respectively. Outside the colluvial transport process domain are conditions outside the regression analysis; therefore, vegetated areas were assigned a depth of 0.5, 1, and 2 m for herbaceous, shrubland, and forest, respectively, to generate a contiguous soil depth map for NOCA consistent with SSURGO. Areas with barren land cover were assigned a soil depth of 0.05 m, representing the minimum range of modeled herbaceous areas. Developed areas were assigned a value of 0.5 m. Areas assigned a such fixed value are about 2% of the model domain.

As an alternative to the SSURGO-SD, the map of the mode values of M-SD was used to represent the most likely soil depth at each grid cell in the landslide probability model. The evolved soil depth was also used to revise *T*, using the *Ks* provided by SSURGO, which provides a more-distributed continuous field of *T*. The revised T map is used when Landlab is run based on mode from M-SD.

Local erosion is calculated within the soil evolution model. Calibration of the soil evolution model was performed by adjusting model parameters from the literature (e.g., Tucker and Slingerland, 1997; Nicótina et al., 2011) and comparing the mean annual rock erosion rate estimated by the model to long-term average rock erosion rates published for the Cascade Mountains, which range from 0.02 to 0.5 mm y^{-1} over roughly the last several Ma (Reiners et al., 2002, 2003) and slightly higher rates over the last millennia of 0.08 to 0.57 mm y^{-1} (Moon et

Earth Surf. Dynam. Discuss., https://doi.org/10.5194/esurf-2017-39
Manuscript under review for journal Earth Surf. Dynam.
Discussion started: 21 June 2017

al., 2011). In addition to published erosion rates, the resulting soil depths were compared to the SSURGO-SD, which ranged from 0.09 to 2.01 m across NOCA.

Modeled erosion rates ranged from 0.037 to 0.49 mm y^{-1}, consistent with published rates as determined by mineral cooling ages (Reiners et al., 2002, 2003; Moon et al., 2011). In Fig. 6 we show modeled mean annual erosion rates in relation to modeled mode soil depth for a steep and moderate slope class, and illustrate the local variability of M-SD under forest and shrub conditions. The relative frequency histogram of soil depth resembles a triangular distribution, with mode values generally higher than mean values, indicating a negatively (left) skewed distribution for soil depth (Fig. 6a, 6c). Therefore, there is a higher frequency of deeper soil relative to shallower soils for a given soil distribution. Soil creep fills hollows, thickening soils, as FS gradually drops, leading to episodic landslides that evacuate sediment (Fig. 6b, 6d).

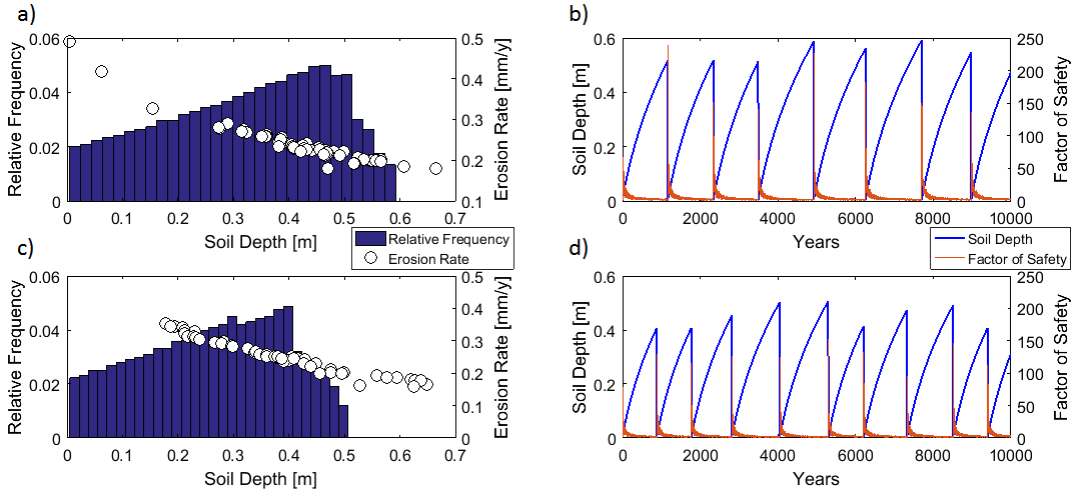

Figure 6. Illustration of the soil evolution model run using **(a, b)** steep slope class and forest vegetation and **(c, d)** moderately steep slope class and shrub vegetation. (a, c) Modeled mean annual erosion rates plotted with respect to soil depth, along with soil depth histogram for a representative convergent location. (b, d) Temporal evolution of soil depth and FS for a representative convergent location with: (a) S=40° and Curv=-0.01; and (b) S=29° and Curv=-0.01.

Comparison of the SSURGO-SD with the M-SD indicates that there is value in a long-term geomorphic perspective in supplying a spatio-temporal soil depth. M-SD exhibits substantially more spatial variability than the SSURGO-SD (Fig. 7). While both soil depth distributions have similar median values, M-SD has a wider distribution with a higher proportion of shallower and deeper soils than SSURGO-SD. In general, the M-SD is shallower than SSURGO-SD on steeper, convex hillslopes with herbaceous or shrub vegetation and deeper on gentler, concave hillslope with forest vegetation. For both models, soil depth is greater in the valleys and shallower near the ridge tops (Fig. 7c, d), consistent with other reporting (Anagnostopoulos et al., 2015; Montgomery and Dietrich, 1994).

Earth Surf. Dynam. Discuss., https://doi.org/10.5194/esurf-2017-39
Manuscript under review for journal Earth Surf. Dynam.
Discussion started: 21 June 2017

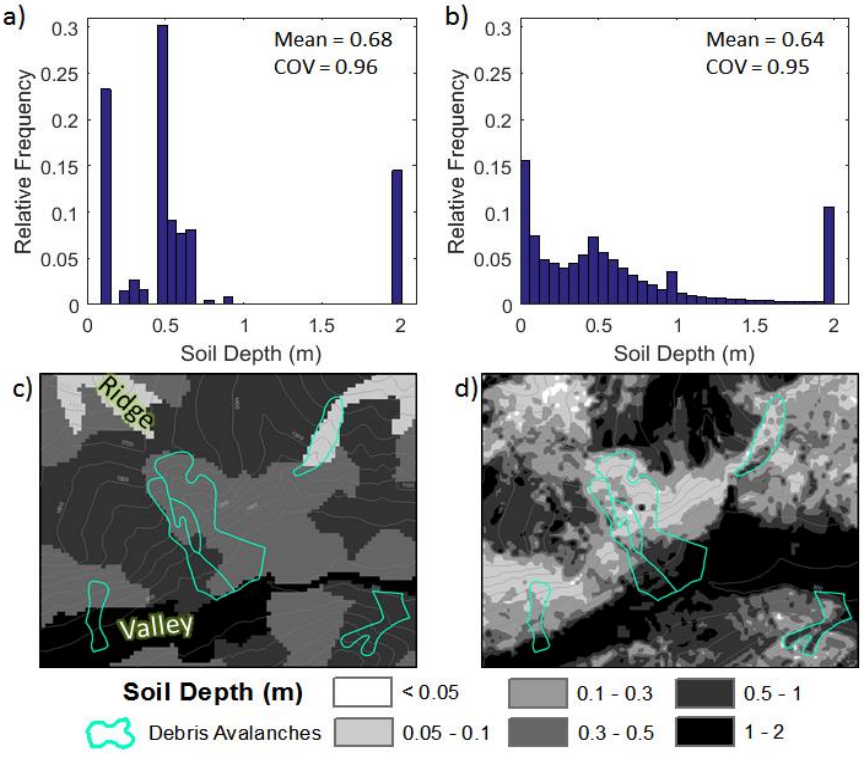

Figure 7. Relative histograms of soil depths within NOCA: **(a)** SSURGO-SD and **(b)** mode of M-SD, with respective spatial mean and coefficient of variation (COV). Example location (~6 km^2) within NOCA: **(c)** SSURGO-SD and **(d)** M-SD. Mapped debris avalanches are outlined in cyan and contours are at 100-m.

The maximum and minimum soil depth parameters of the triangular distribution to characterize soil depth variability were obtained by analyzing soil evolution model results. At most θ, CA, and Curv triplets using in the soil evolution model, a landslide occurred at least once. Given the negatively-skewed nature of the temporally evolved soil depth, maximum evolved soil depth was set equal to 10% of the mode in all model simulations. Two M-SD scenarios were developed to compare with SSURGO-SD reflecting existing contemporary and long-term soil depths. In SSURGO-SD and M-SD simulations we set the minimum parameter as 70% of the mode. However, for a long-term evolved soil depth (M-SD LT), if the minimum was greater than 0.005 m, the minimum soil depth was set to 0.005 m, reflecting the effect of landslides over a long term. This introduces a temporal uncertainty component to modeling landslide probability, which can be used to more accurately estimate landslide return period.

4.2 Probability of Failure

Modeled annual probability of failure of shallow landslides, P(F), for NOCA simulated by the Landlab LandslideProbability component using SSURGO-SD and two M-SD scenarios are shown in Fig. 8. In each run 3,000 values were sampled for model parameters at each grid cell in the Monte Carlo simulations.

Earth Surf. Dynam. Discuss., https://doi.org/10.5194/esurf-2017-39
Manuscript under review for journal Earth Surf. Dynam.
Discussion started: 21 June 2017

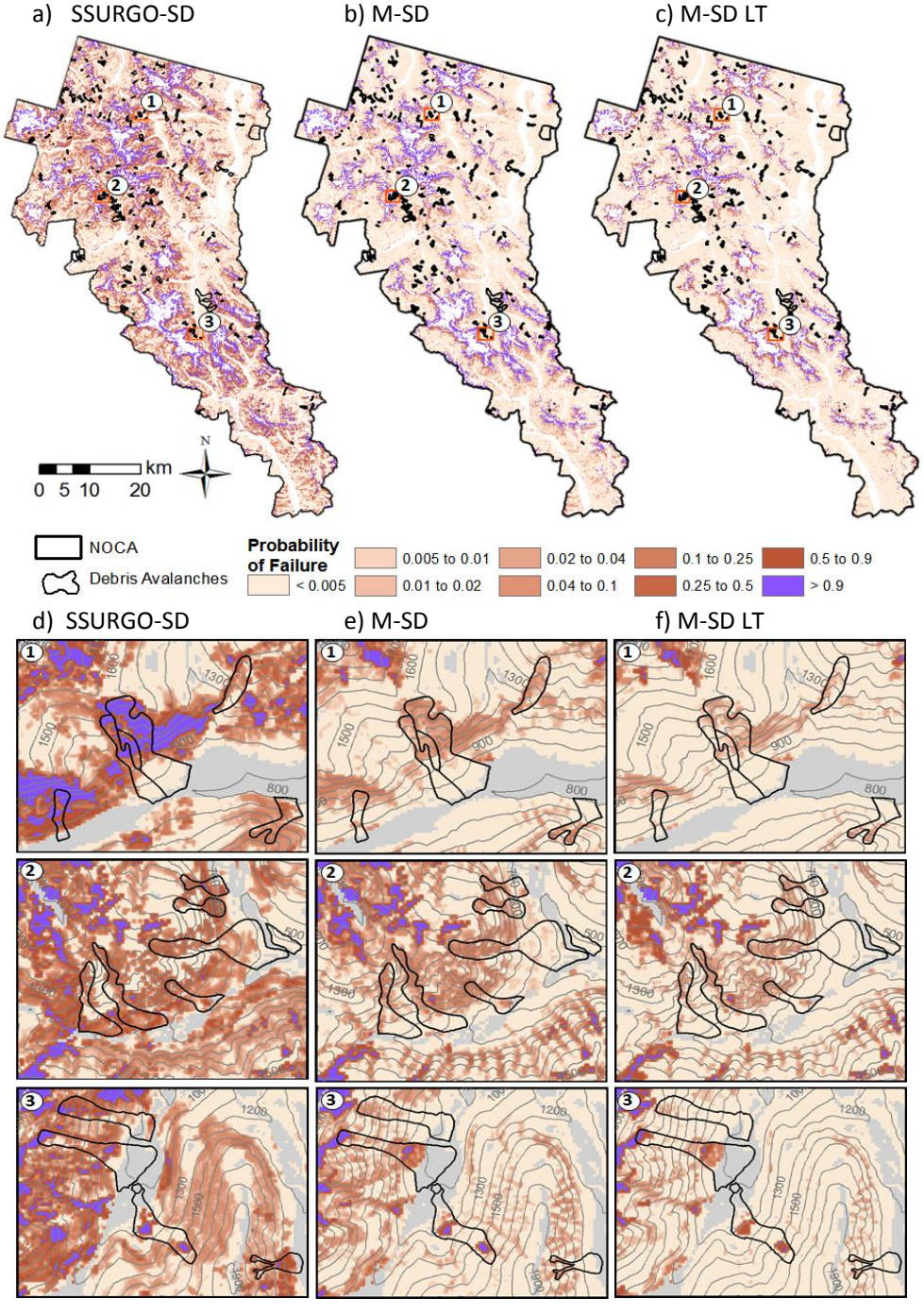

Earth Surf. Dynam. Discuss., https://doi.org/10.5194/esurf-2017-39
Manuscript under review for journal Earth Surf. Dynam.
Discussion started: 21 June 2017

Figure 8. Landslide annual P(F) map for NOCA overlain with mapped debris avalanches for simulations with: **(a)** SSURGO-SD; **(b)** M-SD; **(c)** M-SD LT. Zoomed-in areas are shown for greater detail in the lower panel in the same order and according to number designated. Purple areas are considered chronically unstable and areas excluded from analysis are shown as gray. Contours are at 100 m. Aerial images of zoomed-in areas are provided in Fig. 3.

P(F) derived from simulations exhibit low probabilities where slopes are moderate and cohesion is high (e.g., forest). Highly unstable areas largely correspond to steep barren landscape mostly located below retreating alpine glaciers, with steep glacial landforms, transitioning from glacier to colluvial processes (similar to Guthrie and Brown 2008; Tarolli et al., 2008; Legg et al., 2014) (Fig. 9). Barren areas cover ~13% of the modeled domain. These areas with a thin veneer colluvium, except for moraines, appear to be "continuously sliding" (Borga et al., 2002) or "chronically unstable" (Montgomery, 2001), which also impedes the colonization of vegetation (Dietrich et al., 1995; Istanbulluoglu and Bras, 2005). Shallow soils can enhance the probability of saturation, leading to high pore-water pressure and saturated overland flows with moderate storms (Pelletier and Rasmussen 2009). Mass wasting activity in barren areas were not completely included in our landslide inventory as they exhibit chronic small-scale slides that do not pose major risks or substantial deposition zones.

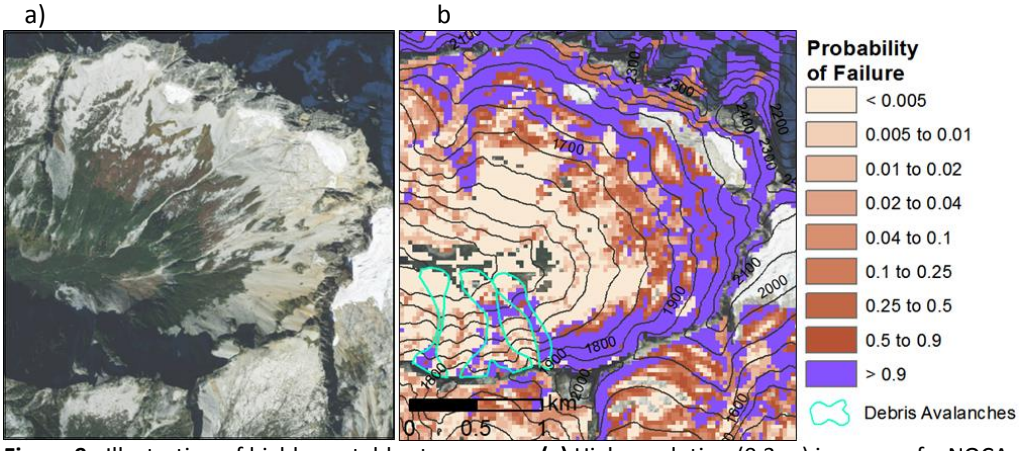

Figure 9. Illustration of highly unstable steep areas: **(a)** High resolution (0.3 m) imagery of a NOCA mountain (World Imagery, Esri Inc.)[1] compared to **(b)** P(F) simulated by M-SD with mapped debris avalanches. Contours at 100 m. Notice the barren areas below retreating glaciers with high P(F).

Other locations of higher P(F) are located in topographic hollows (Fig. 8, 9). These converging areas accumulate deeper soils, which decreases the effectiveness of root cohesion, and attract subsurface flow, leading to enhanced pore-pressure (Dietrich et al., 1995). Converging areas often correspond to the upper portions of mapped debris avalanches, which display higher landslide probabilities than the runout portions in simulations. Thus, the landslide probability visually appears to capture the source area of debris avalanches.

Substantial differences between P(F) derived with different soil depth maps are evident (Fig. 8 and Fig. 10) and corroborate previous studies showing the influence of various soil depth estimates on landslide susceptibility (Dietrich et al., 1995; Okimura, 1998). In general, probabilities are higher and more spatially extensive when the model is parameterized using SSURGO-SD compared to both M-SD scenarios. Given that other parameters are kept consistent, these differences are attributed to spatial variability of soil depth and related adjustments to transmissivity.

To investigate the spatial distribution of P(F) in relation to soil depth, we plot the cumulative distribution of P(F), referred to as the fraction of modeled area where P(F) is less than or equal to a given value, for each simulation (Fig 10a). We present our general observations of the spatial distribution of P(F) in the order of SSURGO-SD, M-SD, and M-SD LT as depicted in Fig 8. Simulations show approximately 26%, 38%, and 49% of the modeled domain (79% of NOCA, where θ>17°) as stable (i.e., P(F)=0) under the current vegetation cover and climate. We refer to these sites as unconditionally stable (i.e., stable even when saturated, and with minimum C and ø sampled) (Pack et al., 1998; Montgomery 2001). A bimodal spatial distribution for P(F) is evident (Fig. 10a, 10b). Areas with low probabilities, around P(F)≤0.1, dominate the spatial distribution of P(F), manifested with a steep rise in the fraction of area from P(F)=0 to P(F)=0.1 (Fig 10a). For P(F)≤0.1 (RP≥10 years), the order of aerial cover for the model domain, including the stable regions, is 72%, 85%, and 87%. When the unconditionally stable areas are excluded, the percentages become 46%, 47% and 38%, respectively, for the three soil depth products used. This region approximately marks the first peak of the relative histogram of P(F) (Fig. 10b). In the broad 0.9>P(F)≥0.1 range, the increase in fraction of area with P(F) is gradual especially for the two M-SD simulations (Fig. 10a). In the highly unstable regions, with P(F)≥0.9 (RP≤1.1) as mapped in Fig. 8 and 9, the fractional area begins to rise again in all simulations (Fig 10a). P(F)=1 occupies 11% and 7% of the modeled area in the SSURGO-SD and M-SD simulations, which can be conceptually named as unconditionally unstable (i.e., unstable even when dry and with the highest combinations of C and ø sampled) (Pack et al., 1998; Montgomery 2001). The model run using M-SD LT soil scenario shows a smaller area percentage, ~6%, with P(F)≥0.9, while SSURGO-SD and M-SD had 16% and 10%. M-SD LT soil scenario provides a more realistic estimate as some locations are not likely to produce slope failures annually due to limited soil development. The second peak of the relative frequency histogram of P(F) appears when P(F)>0.9, largely associated with postglacial barren lands with steep mountain slopes, and converging topography, especially in the case of SSURGO-SD (Fig. 10b). Dominant factors that control the relative frequency of P(F) are labeled in Fig 10b, and further discussed in subsequent sections.

Earth Surf. Dynam. Discuss., https://doi.org/10.5194/esurf-2017-39
Manuscript under review for journal Earth Surf. Dynam.
Discussion started: 21 June 2017

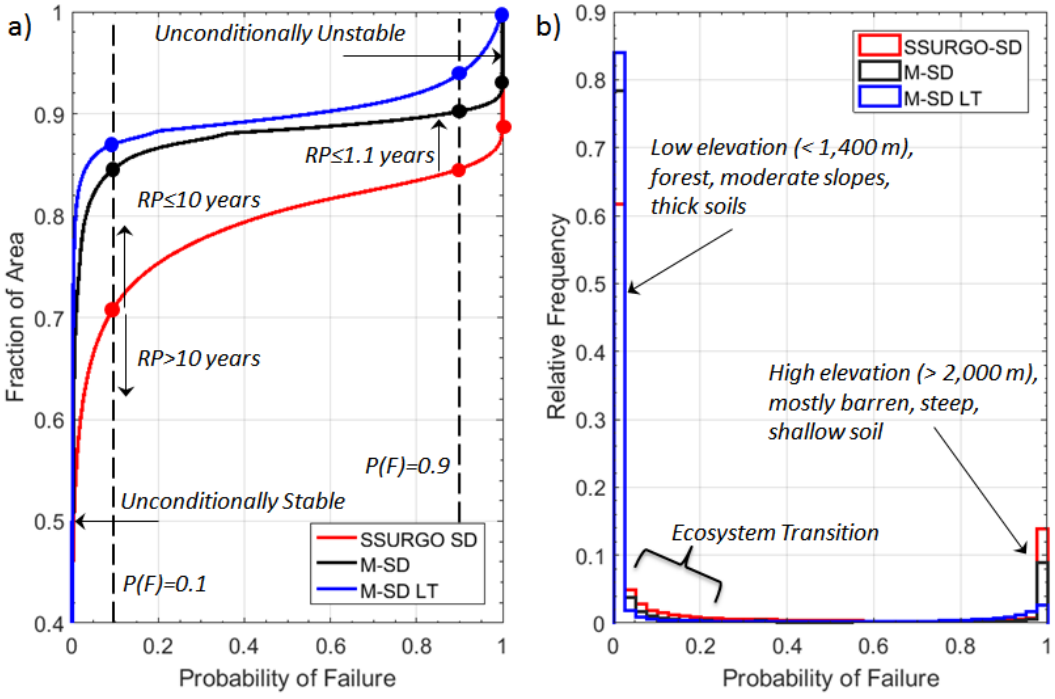

Figure 10. (a) Cumulative distribution and **(b)** relative frequency of P(F) (bin size ΔP(F)=0.025) mapped over NOCA from Landlab simulations using SSURGO-SD and two M-SD scenarios. Labels indicate dominant controls on the distribution of P(F) in (b). Fraction of area is used for cumulative spatial probability, plotted using the Weibull plotting position. Return Period for landslides are illustrated only for SSURGO-SD.

We expressed the annual probability of landsliding in the form of a RP, plotted with respect to fraction of area for all three simulations, and mapped RPs for the M-SD LT scenario in Fig. 11. The M-SD LT reduces the probability and increases the return period estimates of landslide initiation, revealing the influence of long-term memory of landsliding on the probability distribution of soil thickness obtained from the soil evolution model. Therefore, the M-SD LT scenario would better suit the definition of RP, while the other two simulations provide reference for relative comparisons. In general and in concert with the P(F), landslides at nearly all RPs affect a greater proportion of the domain when SSURGO-SD is used. Approximately 28% of the model domain is simulated to have a landslide return period of less than or equal to 10 years (i.e., P(F)≥0.1 or frequent slides) based on SSURGO-SD, compared to half as much area, 15%, for simulations using M-SD; M-SD LT had slightly less at 13%. Low return periods (i.e., < 10 years) coincide with steep slopes in barren areas that show chronic landsliding, low-cohesion vegetation type, such as herbaceous, as well as some steep hollows.

At the high end of the return period, 46% of the model domain was simulated to have landslides with a return period of ≥500 years for SSURGO-SD scenario, including stable areas,

Earth Surf. Dynam. Discuss., https://doi.org/10.5194/esurf-2017-39
Manuscript under review for journal Earth Surf. Dynam.
Discussion started: 21 June 2017

compared to 52% and 70% for model runs that used M-SD and M-SD LT scenario, respectively (Fig. 11). High return periods (i.e., RP>500 years, P(F)< 0.002) are found where slopes are gentler, on divergent topography, and in forest areas. The fraction of the model domain with a landslide return period between 100 and 500 years is 10%, 18%, and 21% for SSURGO-SD, M-SD, and M-SD LT, respectively, showing a larger fraction in the M-SD products. These landslide frequency rates relate to long-term averages and the actual failures are likely to be clustered in space and time depending on triggering event and the time since the last landslide at the same location (Guthrie and Evans, 2004).

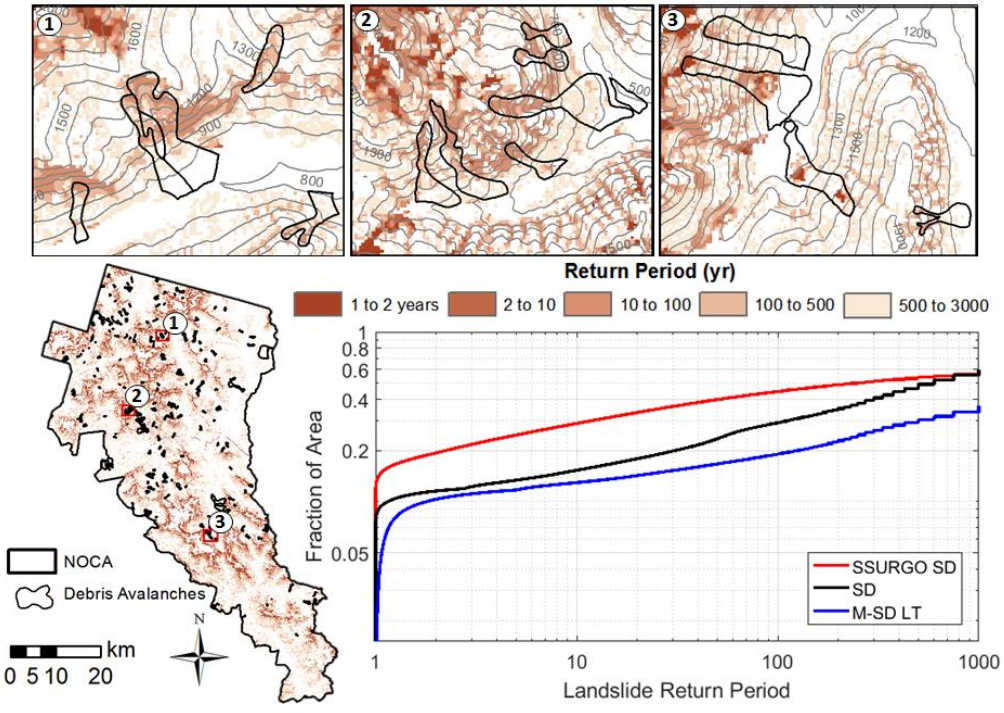

Figure 11. Modeled landslide return period simulations with M-SD LT for NOCA overlain with mapped debris avalanches, including zoomed in areas at top for greater detail. Cumulative distribution of return periods for SSURGO-SD, M-SD, and M-SD LT scenarios, plotted on a log-log scale using the Weibull plotting position.

As soils in landslide locations are formed by sediment accumulation from surrounding hillsides and weathering of the local bedrock, landslides can be the main source of denudation across landslide-prone regions. The expected values of mean annual denudation rate is approximated by: mean(P(F)*h_s)/(ρ_r /ρ_s) for each simulation. This gives spatial average of the long-term denudation rates due to landslides as 51.9 mm y^{-1}, 7.06 mm y^{-1}, and 5.04 mm y^{-1} for SSURGO-SD, M-SD, and M-SD-LT scenarios, respectively. While these rates are higher than the reported mean annual denudation rates in this region over the last millennia of 0.08 to 0.57 mm y^{-1} (Moon et al., 2011), M-SD-LT clearly gives the closest estimates to observations among the

Earth Surf. Dynam. Discuss., https://doi.org/10.5194/esurf-2017-39
Manuscript under review for journal Earth Surf. Dynam.
Discussion started: 21 June 2017

three soil depth scenarios. Over an order of magnitude variation in denudation rates is also common as part of long-term records of erosion rates (e.g., Molnar, 2004).

A critical question that remains is: what are the dominant controls that lead to the bimodal distribution of landslide probability in the modeled domain? First, we examined if topography alone, represented by S and CA pairs, can explain this behavior. The S-CA data pairs from each model grid cell are colored by the value of P(F) in the order from low to high value using output from the M-SD LT scenario (Fig. 12). As slopes get steeper (S>0.45 or 24.2°), a relatively rapid increase in P(F) in relation to slope from 0.4 to 1.0 can be seen, surrounded with lower probabilities. CA does not seem to impose a visually detectable increase in P(F), which is likely largely due to the wet climate in region. The landslide source cells identified from the highest elevation of debris avalanche shapefiles fall in the "eye" of this high-P(F) region in the S-CA domain. Interestingly, P(F) diminishes in the steepest slopes of most CAs. While the trend of increasing P(F) as slope gets steeper generally shows the influence of slope in Eq. (1a), landscape with P(F)≥0.4 only constitute about 11% of the model domain (Fig. 10a). For comparison P(F)≥0.1 was 13%. On the other hand, about 57% of the domain has steeper slopes than 24.2° (S=0.45m/m). Locations with slopes less than this are rarely found with P(F)>0.4. This suggest that the majority of the domain with similar pairs of S and CA exhibit lower landslide probability, which can be largely attributed to the spatial distribution and influence of vegetation type and soil depth (e.g., Roering et al., 2003).

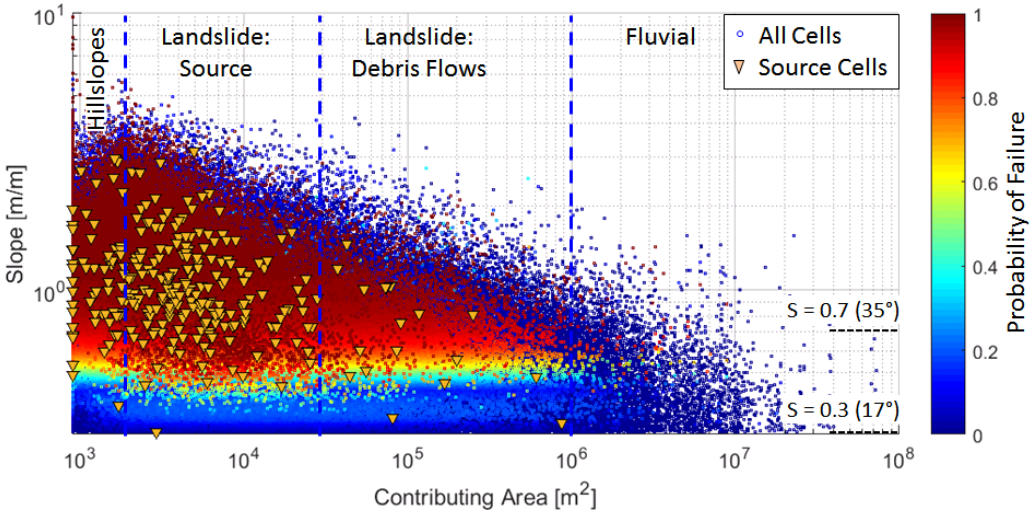

Figure 12. S-CA plot colored by the P(F) simulated with from the M-SD LT. Source cells (orange triangles) are the single highest-elevation grid cell within mapped debris avalanches. Comparable to Fig. 5. High probabilities plot over low probabilities.

We investigated the roles of vegetation, slope steepness, and soil depth on P(F) in relation to elevation (Fig 13). From low to high elevations, vegetation changes from predominantly forest (elevation <1,400 m) to coexisting shrub, herbaceous plants, and barren land (1,400 m to 2,200

m) as a result of elevation-dependent ecoclimatic controls (e.g., temperature) on vegetation survival and growth (Fig. 13a). In this region of ecosystem transition, the mean P(F) shows a persistent increase from 1,400 m until a maximum is reached between 2,200 and 2,400 m, depending on simulation (Fig. 13b, 13c). Observations of debris avalanche by elevation confirm the pattern of P(F) dependence on elevation in relation to ecosystem change; 75% of the extracted landslide initiation zones from mapped debris avalanches are located between 1,200 m to 2,000 m (Fig. 3b). In the 1,400 to 1,900 m elevation range of the ecosystem transition zone, mean slope is relatively constant ~0.75 m/m (~37^{o}), and rises up to 0.9 m/m (42^{o}) between 1,900 and 2,200 m (Fig 13c), consistent with the binned-averaged slopes of the landslide source area in the S-CA plot in Fig 5. Mean soil depth begins to drop in both SSURGO and modeled soil depth products above 2,200 m.

These observations confirm the strong control of ecosystem transition on landslide activity in the region. Below about 1,400 m (~40% of NOCA), forested vegetation combined with deeper soils and moderate slopes keep P(F) low. In the 1,400 to 2,200 m range, loss of root cohesion with ecosystem transition combined with gradual increase in landscape slopes contribute to increased P(F). Above 2,200 m elevation, soils become very shallow and slopes exhibit the steepest angles in the modeled domain. This combination leads to the largest variability in P(F), combining the highest P(F) values, P(F)≥0.9 mostly attributed to barren areas (~6% of the model domain in the M-SD LT scenario), with lower P(F) values where thinner soils reduce the driving force within Eq. (1a). In aggregate, thinner soils at higher elevations lead to lower mean P(F), which we referred to as soil depth control. The general contribution of elevation on the spatial organization of P(F) is labeled in Fig 10b.

Earth Surf. Dynam. Discuss., https://doi.org/10.5194/esurf-2017-39
Manuscript under review for journal Earth Surf. Dynam.
Discussion started: 21 June 2017

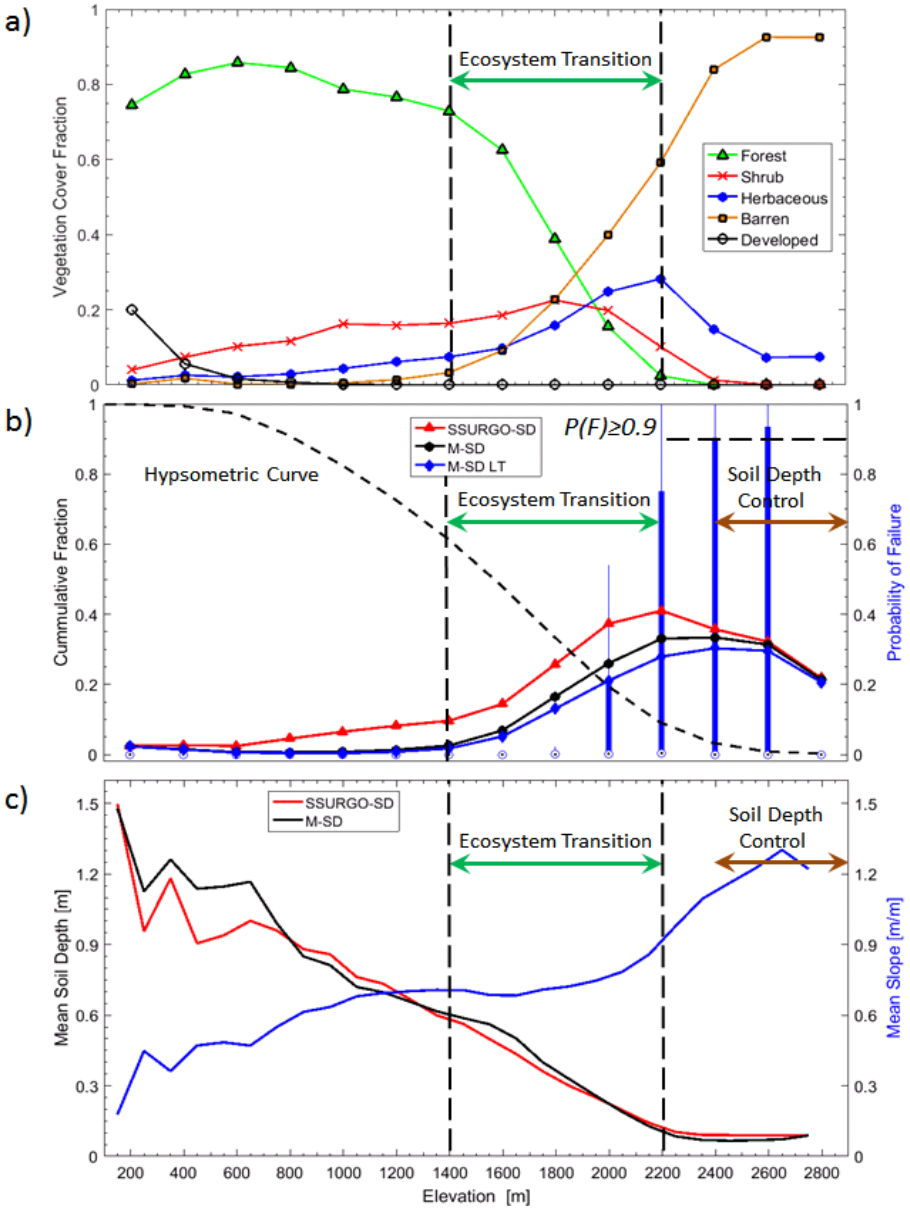

Figure 13. Elevation (200 m bands or bin) influence on: **(a)** vegetation cover fraction for NOCA, taken as fraction of vegetation type within each elevation band, **(b)** mean P(F) using SSURGO-SD and two M-SD scenarios, along with compact box-whisker plots for P(F) of M-SD LT scenario where circles-dot symbol represents median (outliers not shown, greater than 1.5 interquartile distance) overlaid with hypsometric curve for NOCA, and **(c)** mean soil depth for SSURGO-SD and M-SD products with mean slope. Mean values calculated within each 200-m elevation band.

Earth Surf. Dynam. Discuss., https://doi.org/10.5194/esurf-2017-39
Manuscript under review for journal Earth Surf. Dynam.
Discussion started: 21 June 2017

4.3 Model Evaluation

The performance of a landslide model is often based on its ability to capture existing mapped landslides. In Sect. 4.2 we evaluated our model through visual comparison of modeled P(F) to observed landslide locations (e.g., Fig. 8, 9). In this section, a more quantitative approach is presented for model evaluation. We statistically evaluated our model using multiple approaches, including cumulative distribution (CD) of P(F) comparisons as well as Receiver Operating Characteristics (ROC) (Fawcett, 2006) and Success Rate (SR) curves (Bellugi et al., 2015).

For the statistical analysis, we limited our performance assessment to the source areas of the mapped debris avalanches. Source areas of debris avalanches were not mapped separately from the remaining debris avalanche features (i.e., transition and deposition zones) hindering the evaluation of model predictions (Tarolli and Tarboton, 2006). Because we anticipate that the source areas could originate from a neighboring grid cell, we considered source cells as a collection of grid cells in the upper 10, 20, and 30% highest elevation cells within each mapped debris avalanche shapefile. These populations of source cells were treated as 'observed' landslide source cells during validation of the landslide probability using CD, SR and ROC performance metrics. In this validation, we excluded barren areas with slopes ≥ 37° (~5% of the model domain), which characterizes slopes of active small-scale dry landslides (failure depth ≤ soil depth) more appropriately represented by nonlinear hillslope diffusion models (see Roering et al., 1999; DiBiase et al., 2010; Pelletier et al., 2013).

For comparison of P(F) with source area cells, we randomly sampled 50,000 grid cells outside mapped debris avalanches (~2% of the modeled domain), similar to the number of grid cells within entire mapped debris avalanche areas. The majority of the source grid cells and outside debris avalanches cells are located at elevations between 1200 and 1800 m (Fig. 14a). Grid cells in the random sample outside debris avalanches were constrained to the elevation range of the source cells to allow unbiased comparison. We recognize that the areas outside mapped debris avalanches have the potential to be unmapped landslides, other landslide types, or unstable areas deficient a triggering event; therefore, we interpret the test results conservatively. We expect the simulated P(F) should estimate lower probability outside debris avalanches compared to source areas of mapped debris avalanches.

At low and mid elevations, simulations generally showed a greater fraction of high probabilities in source areas compared to outside of debris avalanches (Fig. 14b, c). However, when only high elevation (>1,800 m) data were considered, the pattern was reversed with a larger fraction of high probabilities found outside debris avalanches than source areas (Fig. 14d). At this higher elevation, much of the land cover is barren or herbaceous (i.e., low root cohesion), resulting in high probabilities of failure throughout the model domain (Fig. 12a). While there are extensive shallow failures in these regions only limited amount of those that turned into debris avalanches were mapped. This reverse pattern is also present at mid-elevations (~1,200 to 1,800) for both M-SD scenarios, only for 10% of the sample data, when P(F)>0.03 and

Earth Surf. Dynam. Discuss., https://doi.org/10.5194/esurf-2017-39
Manuscript under review for journal Earth Surf. Dynam.
Discussion started: 21 June 2017

P(F)>0.1 for M-SD and M-SD LT, respectively (note the crossing curves in Fig. 14b). At low elevation (~125 to 1,200 m), there were no source areas with P(F)>0.4 in M-SD and M-SD LT scenarios.

The performance of the model results we are presenting in this paper are specific to a sample comparison of 10% source area of mapped debris avalanches and random sampling outside debris avalanches. When examining the validation datasets in their entirety (i.e., regardless of elevation), the median P(F) of the 10% source DA cells is 13 times the median P(F) of outside DA for SSURGO-SD and four times the median P(F) for M-SD; median is zero for outside DA cells in the M-SD LT. The Kolmogorov-Smirnov test (Chakravart et al., 1967) test show paired comparison between DA source area cells and cells outside DA for all three scenarios are statistically different (p<<0.01).

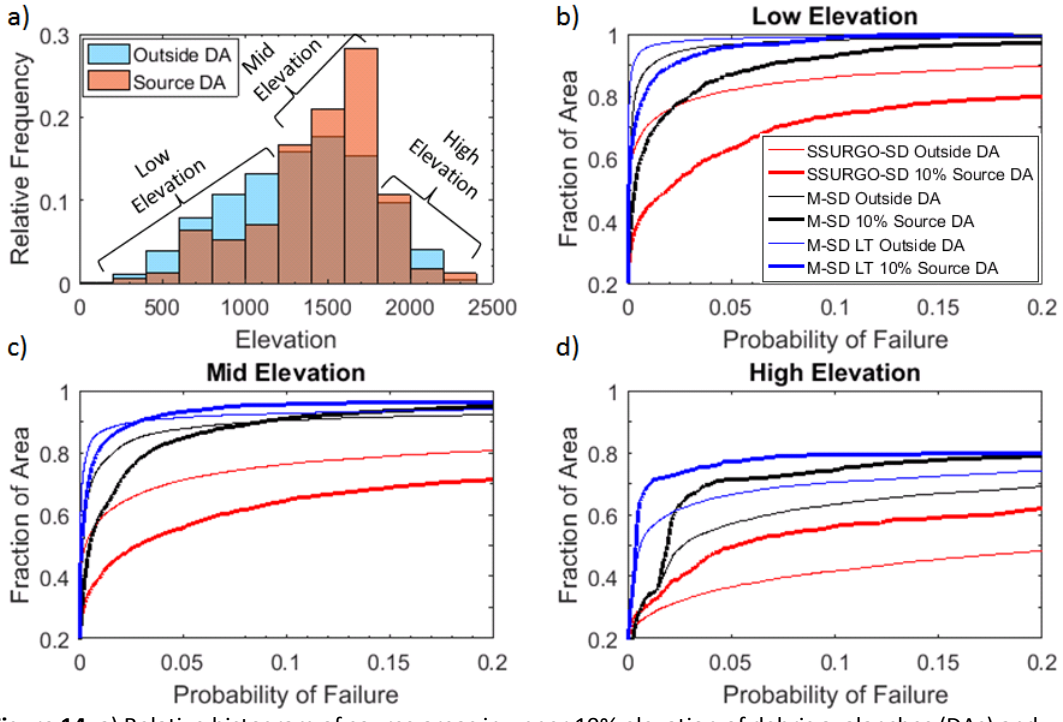

Figure 14. a) Relative histogram of source areas in upper 10% elevation of debris avalanches (DAs) and for 50,000 grid cells outside DAs. Cumulative distributions of P(F) plots limited to P(F) ≤ 0.2, or return period ≥ 5 years, to highlight detail in simulation using SSURGO-SD, M-SD, and M-SD LT at: b) low (<1,200 m), c) mid (1,200 to 1,800 m), and d) high (>1,800 m) elevations as depicted in a). Thicker lines represent probabilities for source areas of (DAs) and thin lines represent probabilities for cells outside DAs.

Another statistical analysis uses ROC curves to examine how our model compares with randomly distributed landslides over the landscape. These curves are constructed from confusion matrices generated from comparisons between observed and modeled landslides,

based on varying P(F) threshold (e.g., 0.1, 0.2, 0.3, etc.). True positives (TP) are those cases within observed landslides where probabilities are equal to or greater than threshold. False negatives (FN) are probabilities within landslides that fall below the threshold. False positives (FP) occur outside observed landslides with simulated probabilities equal to or above the threshold. True negatives (TN) are also outside observed landslides, but with probabilities below the threshold. From these metrics, true positive rate (TPR) or fraction of landslides captured and false positive rate (FPR) or fraction of false alarms can be calculated as follows:

$$TRP = \frac{TP}{(TP+FN)} \quad (8)$$

$$FRP = \frac{FP}{(FP+TN)} \quad (9)$$

The advantage of the ROC curve over a standard confusion matrix is the ability to vary the probability threshold for assigning model simulations to a modeled landslide (positive) or no landslide (negative) classification, generating different positive and negative comparisons (Mancini et al., 2010; El-Ramly et al., 2002; Anagnostopoulos et al., 2015). A better performing model will exhibit a curve toward the upper left of a FPR (x-axis) and TPR (y-axis) plot. A 1:1 line in the plot represents a trivial model that randomly assigns stable and unstable cells. The area under the curve (AUC) generated by ROC curve quantifies the performance of a model for identifying landslide and non-landslide locations. The AUC statistic represents the probability of correctly ranking a landslide and non-landslide pair randomly selected from those two datasets (Hanley and McNeil, 1982). SR curves are similar to ROC curves, with TPR as the y-axis, but compares this to the fraction of landscape predicted as unstable (x-axis), calculated as (TP+FP)/(TP+FP+TN+FN). Again, a relatively well performing model would plots farther away from the 1:1 line representing a trivial model.

For this comparison, we used the same datasets used in the cumulative probability analysis discussed Sect. 4.2. Both simulations using SSURGO and M-SD modeled 10% source areas and non-landslide areas better than random selection as demonstrated by the curves plotted above the 1:1 line (Fig. 15). The classification is stronger as the source area fraction is reduced. However, the model's strength in the classification is modest as indicated by the AUC values of between 0.60 and 0.61, compared to an AUC of 1 representing a perfect classification. The TRIGRS-P probabilistic landslide model tested by Raia et al. (2014) found higher AUC results (i.e., 0.65 to 0.73). However, their study tested small areas (3 to 6 km^2) that were well studied locations with detailed inventories of landslides resulting from one or two winter rainfall seasons and the entire landslide was tested rather than source areas only.

Earth Surf. Dynam. Discuss., https://doi.org/10.5194/esurf-2017-39
Manuscript under review for journal Earth Surf. Dynam.
Discussion started: 21 June 2017

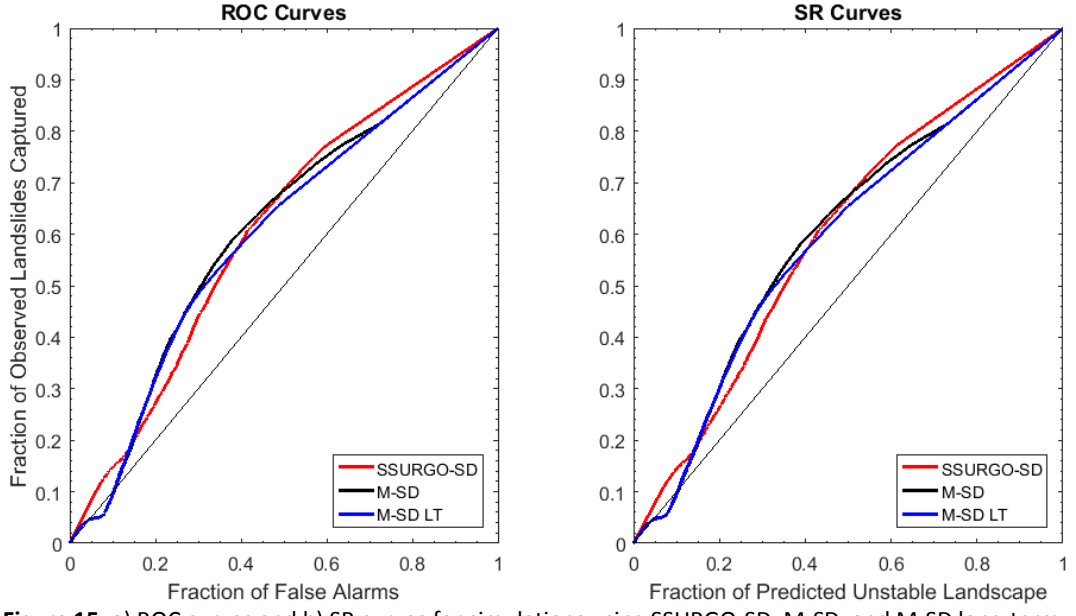

Figure 15. a) ROC curves and b) SR curves for simulations using SSURGO-SD, M-SD, and M-SD long-term (LT). Comparison represent P(F) for the upper 10% of DA as observed landslides to a random sample of 5,000 cells outside DAs. Thresholds for simulated probabilities associated with positive classification of a source areas declines along the curves from lower left to upper right. Black diagonal line on a 1:1 line represents the case of a trivial or random classification model.

ROC and SR curves provide an indication of how well the modeled simulations of P(F) classify both observed landslide source cells and non-landslide grid cells compared to random classification. The crossing of ROC and SR curves in the simulations with M-SD (Fig. 15) implies that at higher probability thresholds, simulated probabilities delineate more false alarms (e.g., areas outside DAs as unstable) than capturing source areas. This may be indicative of the high probability values at high elevations even outside the debris avalanches where vegetation is sparse, as was indicated above in the analysis of cumulative distribution plots. We found for our case study that the optimal probability threshold to maximizing landslides captured and minimizing false alarms (i.e., point around the apex of the ROC curves) declines by half depending on the simulation: P(F)≥0.008 (i.e., RP≤125 years) for SSURGO-SD, P(F)≥0.004 (i.e., RP≤250 years) for M-SD, and P(F)≥0.002 (i.e., RP≤500 years) for M-SD LT.

The modeled potentially unstable landscape has generally been greater than observed landslides when infinite slope stability models are calibrated with limited observations (Sidle and Ochiai, 2006; Baum et al., 2010). As pointed out by Borga et al. (2002), concluding "overrepresentation" of areas potentially subject to shallow landsliding can be misleading because the absence of mapped landslides does not necessarily indicate an absence of landslide hazard over time across the landscape. Locations with high landslide probability

outside mapped landslides in both simulations could be indicators of where to conduct additional investigations for missed landslides or areas on the verge of failing.

Validating hazard maps is challenging, especially in large areas of remote mountainous regions, because inventories are typically incomplete, lack the date of landslide occurrence, different landslide types likely have different meteorological triggers, environmental conditions change after a landslide event, and unidentified high probability areas may fail in the near future even though they appear to be stable during an inventory (van Westen et al., 2006;Tarolli and Tarboton, 2006). Additional evaluation of model performance would benefit from field investigation in areas of high and low modeled P(F) to identify any landslides or instability that may have been missed during the original inventory. Future work that couples the volume of sediment available for landsliding will lead to further improvements in estimating hazards and potential impacts from landslides.

4.4. Model Limitations

For model design and computation efficiency, we made several simplifying assumptions. We neglect groundwater leakage to the bedrock in recharge estimation and apparent soil cohesion through the effect of surface tension in unsaturated zones, both of which could be added to future updates to the component. Tree and snow surcharge is also disregarded, although it may have some stabilizing effect where soils are shallower than 1 m (Hammond et al. 1992). Our approach does not simulate the actual number of landslides, landslide type, nor the size of the landslide because the discretized nature of the failure field precludes specific knowledge of which and how many grid units may be involved in a failure at a particular time. These model omissions present opportunities for future customization of the component or coupling with other models.

Modeled probability does not capture the runout of debris avalanches, which can travel considerable distances in steep mountainous environments. Some unexpected results depicted higher probability in runout portions of some debris avalanches when using SSURGO-SD, but these probabilities were lower when M-SD scenarios were used (e.g., Fig. 8, middle zoomed-in panels). Mis-mapping of probabilities of failure and observed landslide are likely attributed to variations in soil depth, material properties, and hydrologic routing (Schmidt et al., 2001). Model parameters such as slope derived from DEMs developed with post-landslide mapping can also contribute to reduced probabilities in observed landslides where slope and soil depth were reduced. Furthermore, inventories over broad areas are challenging as landslides are isolated processes that may occur with regularity, but may not be large in size (Van Westen et al., 2006). Finally, steady-state flow that we used for subsurface flow neglects transient processes and roles of macro-pores. Macropores from decayed roots or animal activity can be important in transporting water relatively quickly from the surface to deeper soil layers and groundwater (Sidle et at., 2001; Gabet et al., 2003; Beven and Germann 2013).

Earth Surf. Dynam. Discuss., https://doi.org/10.5194/esurf-2017-39
Manuscript under review for journal Earth Surf. Dynam.
Discussion started: 21 June 2017

5 Conclusion

We develop a regional model of probabilistic shallow landslide initiation based on the infinite slope stability equation coupled by steady-state subsurface hydrology driven by groundwater recharge. Uncertainty in model parameters is explicitly accounted for through Monte Carlo simulation. A geomorphic soil evolution model provides a spatially-distributed soil depth alternative to homogeneous patches of soil depths provided by SSURGO. This feature allows the landslide model to be used where soil depth information is uncertain, sparse, or absent. Our model developed in Landlab (Hobley et al., 2017) is made up of a landsliding component, a Landlab utility for hydrologic data processing, and a model driver that runs the component. The model driver can be run on personal computers or online via Hydroshare through cloud computing creating reproducible results. Our approach demonstrates:

- Regional maps of landslide hazard produced with three different soil depth scenarios reveal alternative simulations of probability of landslide initiation, reflecting the importance in soil depth in landslide hazard prediction.
- Simulations using SSURGO-SD returned higher probability of failures and shorter return periods than simulations using modeled soil depth products (M-SD and M-SD LT). The M-SD LT simulation further reduces the probability of failure and increases the return period. Mean annual denudation estimates from the M-SD LT scenario show closer estimates to published rates of denudation over the last millennia than the other simulations.
- SSURGO-SD scenario provide a short-term tool for high risk planning using conservative estimates of probability of failure, while M-SD LT provides long-term estimates more consistent with landslide frequency in the region and useful for management of ecosystems and aquatic habitats, and estimation of sediment budgets for watershed planning.
- Elevation dependent patterns in probability of landslide initiation show the stabilizing effects of forests in low elevations, an increased landslide probability with forest decline at mid elevations (1,400 to 2,400 m), and soil limitation and steep topographic controls at high alpine elevations and post-glacial landscapes. These dominant controls manifest in a bimodal distribution of spatial annual landslide probability, modes controlled by highly stable forested and chronically unstable post-glacial domains and other barren areas.
- Model testing with limited observations revealed similar model confidence for the three hazard maps, suggesting suitable use as relative hazard products. Validation of the model with observed landslides is hindered by the completeness and accuracy of the inventory, estimation of source areas, and unmapped landslides.
- Our shallow landslide hazard model provides regional scale estimates of the relative annual probability of shallow landslide initiation as well as landslide return period, which is useful for civil protection through land use planning to minimize geohazard consequences from precipitation triggers.

6 Data and Model Availability

To facilitate ease of use of the landslide hazard model, we developed the landslide model as a component of Landlab, an open-source Python toolkit for two-dimensional numerical modeling of Earth-surface dynamics available at GitHub: http://github.com/landlab/landlab (Hobley et al., 2017). Documentation, installation instructions, and software dependencies for the entire Landlab project can be found at: http://landlab.github.io/. The Landlab project is tested on recent-generation Mac, Linux and Windows platforms using Python versions 2.7, 3.4, and 3.5. The Landlab modeling framework is distributed under a MIT open-source license. A user manual and driver scripts for the application of the Landlab LandsideProbability can be found at: https://github.com/landlab/pub_strauch_etal_esurf (Strauch, GitHub Repository)

Online access to the Landlab LandslideProbability model is freely provided through https://www.hydroshare.org, where data and code drivers are available to demonstrate and explore the model using interactive IPython notebooks in a JupyterHub. Thus, users can access, test, adapt, and apply the landslide model for their area of interest without downloading Landlab or the components. Data and driver code used in this analysis are available at hydroshare (Strauch et al., 2017). Existing demonstration driver codes can be adapted to fit data provided in raster format by the user to create distributed data fields used as parameters in the component. Instructions for accessing HydroShare and the online demonstrations, codes, and data used in this paper are provided in supplemental material.

Acknowledgements

This research was supported by the US National Science Foundation (CBET-1336725, OAC-1450412) and USGS Northwest Climate Science Center. We thank Dan Miller for helpful review of an earlier version of the manuscript. Technical editing on portions of the manuscript was provided by Brad Strauch and Diann Strom. We also appreciate the developers of Landlab, including open-source contributors to the earth surface processes modeling community. Data repository (Strauch et al., 2017), testing, and online reproducibility was facilitated by the cyber infrastructure of HydroShare services provided by researchers associated with the Consortium of Universities for the Advancement of Hydrologic Science, Inc. (CUAHSI), particularly the support of Tony Castronova, and the team at CyberGIS Center for Advanced Digital and Spatial Studies for their maintenance and support for our use of the ROGER Supercomputer at the National Center for Supercomputing Applications (NCSA) at University of Illinois at Urbana-Champaign.

7 Reference

Adams, J.M., Gasparini, N.M., Hobley, D.E.J. Tucker, G.E., Hutton, E.W.H., Nudurupati, S.S., and Istanbulluoglu, E.: The Landlab v1. 0 OverlandFlow component: a Python tool for computing shallow-water flow across watersheds, Geoscientific Model Development, 10.4, 2017.

Alvioli, M., Guzzetti, F., and Rossi, M.: Scaling properties of rainfall induced landslides predicted by a physically based model, Geomorphology, 213, 38-47, 2014.

Anagnostopoulos, G.G., Fatichi, S., and Burlando, P.: An advanced process-based distributed model

for the investigation of rainfall-induced landslides: The effect of process representation and boundary conditions, Water Resources Research, 51(9): 7501-7523, 2015.

Barling, R.D., Moore, I.D., and Grayson, R.B.: A quasi-dynamic wetness index for characterizing the spatial distribution of zones of surface saturation and soil water content, Water Resources Research, 30.4: 1029-1044, 1994.

Bathurst, J. C., Moretti, G., El-Hames, A., Moaven-Hashemi, A. and Burton, A.: Scenario modelling of basin-scale, shallow landslide sediment yield, Valsassina, Italian Southern Alps, Natural Hazards and Earth System Science, 5.2: 189-202, 2005.

Baum, R.L., Galloway, D.L., and Harp, E.L.: Landslide and land subsidence hazards to pipelines, U.S. Geological Survey Open-File Report 2008-1164, 192 pp., 2008a.

Baum, R., Savage, W., Godt, J.W.: TRIGRS — a fortran program for transient rainfall infiltration and grid-based regional slope-stability analysis, version 2.0, U.S. Geological Survey Open-File Report 2008-1159, 75 pp., 2008b.

Baum, R.L, Godt J.W., and Savage, W.Z.: Estimating the timing and location of shallow rainfall-induced landslides using a model for transient, unsaturated infiltration. Journal of Geophysical Research: Earth Surface, 115(F3), 2010.

Baum, R.L., Schulz, W.H., Brien, D.L., Burns, W.J., Reid, M.E., and Godt, J.W.: Plenary: Progress in Regional Landslide Hazard Assessment—Examples from the USA, In: Landslide Science for a Safer Geoenvironment, Springer International Publishing, 21-36, 2014.

Bellugi, D., Milledge, D.G., Dietrich, W.E., Perron, J.T., and McKean, J.: Predicting shallow landslide size and location across a natural landscape: Application of a spectral clustering search algorithm. Journal of Geophysical Research: Earth Surface, 120(12), 2552-2585, 2015.

Bellugi D., W.E. Dietrich, J. Stock, J. McKean, B. Kazian, and Hargrove, P.: Spatially explicit shallow landslide susceptibility mapping over large areas, Italian Journal of Engineering Geology and Environment, doi: 10.4408/IJEGE.2011-03.B-045, 2011.

Benda, L. and Dunne, T.: Stochastic forcing of sediment supply to channel networks from landsliding and debris flow, Water Resour. Res. 33(12): 2849-2863, 1997a.

Benda, L. and Dunne, T.: Stochastic forcing of sediment routing and storage in channel networks. Water Resour. Res. 33(12): 2865-2880, 1997b.

Berti, M., Martina, M.L.V., Franceschini, S., Pignone, S., Simoni, A., and Pizziolo, M.: Probabilistic rainfall thresholds for landslide occurrence using Bayesian approach, Journal of Geophysical Research 117:F04006, 2012.

Beven K.J. and Kirkby, N.J.: A physically based variable contributing area model of basin hydrology, Hydrological Sciences Bulletin 24: 43-69, 1979.

Beven, K., and Germann, P.: Macropores and water flow in soils revisited. Water Resour. Res., 49(6), 3071-3092, 2013.

Bordoni, M., Meisina, C., Valentino, R., Bittelli, M., and Chersich, S.: Site-specific to local-scale shallow landslides triggering zones assessment using TRIGRS, Natural Hazards & Earth System Sciences, 15(5): 1025-1050, 2015.

Borga, M., Fontana, G.D., and Cazorzi, F.: Analysis of topographic and climatic control on rainfall-triggered shallow landsliding using a quasi-dynamic wetness index. Journal of Hydrology, 268(1): 56-71, 2002.

Borga M., Fontana, G.D., Ros, D.D., Marchi, L.: Shallow landslide hazard assessment using a physically based model and digital elevation data, Environ Geol 35(2–3):81–88, 1998.

Braun, J., Heimsath, A.M., and Chappell, J.: Sediment transport mechanisms on soil-mantled hillslopes, Geology, 29(8): 683-686, 2001.

Caine, N. The rainfall intensity: duration control of shallow landslides and debris flows. Geografiska

Annaler. Series A. Physical Geography, 23-27, 1980.

Carrara, A., M. Cardinali, F. Guzzetti, and Reichenback, P.: GIS technology in mapping landslide hazards. In: Carrara, A. and F. Guzzetti (eds.) Geographical Information System in Assessing Natural Hazard. Kluwer, New York, 107-134 pp., 1995.

Casadei, M., Dietrich, W.E. and Miller, N.L.: Testing a model for predicting the timing and location of shallow landslide initiation in soil-mantled landscapes, Earth Surf. Process. Landforms, 28: 925-950, 2003.

Castranova, T., Dockerfile for the HydroShare-JupyterHub base image, https://hub.docker.com/r/castrona/hydroshare-jupyterhub/ (Accessed April 4, 2017), 2017.

Catani F., Segoni, S., Falorni, G.: An empirical geomorphology-based approach to the spatial prediction of soil thickness at catchment scale, Water Resour Res 46, W05508, 2010.

Chakravarti, I. M., Roy, J.D., and Laha, R.G.: Handbook of Methods of Applied Statistics, Volume I, John Wiley and Sons, pp. 392-394, 1967.

Chen, W., Li, W., Hou, E., Zhao, Z., Deng, N., Bai, H., and Wang, D.: Landslide susceptibility mapping based on GIS and information value model for the Chencang District of Baoji, China, Arabian Journal of Geosciences 7(11): 4499-4511, 2014.

Cho, S.E.: Effects of spatial variability of soil properties on slope stability, Engineering Geology, 92(3): 97-109, 2007.

Chung, C.F., A.G. Fabbri, and Van Western. C.J.: Multivariate regression analysis for landslide hazard zonation. In: Carrara, A. and F. Guzzetti (eds.) Geographical Information System in Assessing Natural Hazard. Kluwer, New York: pp. 107-134, 1995.

Crozier, M.J. Prediction of a rainfall-triggered landslide: A test of the antecedent water status model. Earth Surf. Process. Landforms, 24: 825-83, 1999.

Crozier, M. J. Landslides Causes, Consequences, and Environment, Croom Helm, London, 252, pp.,1986.

Cullen, A.C. and Frey, H.C. Probabilistic techniques in exposure assessment: a handbook for dealing with variability and uncertainty in models and inputs, Springer Science & Business Media, 1999.

DiBiase, R.A., Whipple, K.X., Heimsath, A.M. and Ouimet, W.B.: Landscape form and millennial erosion rates in the San Gabriel Mountains, CA, Earth and Planetary Science Letters, 289, 134–44, 2010.

Dietrich, W.E., R. Reiss, J. Hsu, and Montgomery, D.R.: A process-based model for colluvial soil depth and shallow landsliding using digital elevation data, Hydrological Processes 9: 383-400, 1995.

Dou, H.Q., Han T.C., Gong, X.N., and Zhang, J.: Probabilistic slope stability analysis considering the variability of hydraulic conductivity under rainfall infiltration–redistribution conditions, Engineering Geology, 183:1-13, 2014.

El-Ramly, H., Morgenstern, N.R., and Cruden, D.M.: Probabilistic slope stability analysis for practice, Canadian Geotechnical Journal, 39(3):665-683, 2002.

Elsner, M.M., Cuo, L., Voisin, N., Deems, J.S., Hamlet, A.F., Vano, J.A., Mickelson, K.E.B., Lee S., and Lettenmaier, D.P.: Implications of 21st century climate change for the hydrology of Washington State, Climatic Change, 102 (1-2): 225-260, doi: 10.1007/s10584-010-9855-0, 2010.

Fawcett, T.: An introduction to ROC analysis, Pattern recognition letters, 27(8):861-874, 2006.

Formetta, G., Capparelli, G., and Versace, P.: Evaluating performance of simplified physically based models for shallow landslide susceptibility, Hydrology and Earth System Sciences, 20(11): 4585, 2016.

Gabet, E.J., Reichman, O.J., and Seabloom, E.W.: The effects of bioturbation on soil processes and sediment transport, Annual Review of Earth and Planetary Sciences, 31(1):249-273, 2003.

Gabet, E.J., and Dunne, T.: Landslides on coastal sage-scrub and grassland hillslopes in a severe El Nino winter: The effects of vegetation conversion on sediment delivery, Geol. Soc. Am. Bull., 114(8):983–990, 2002.

Glade, T.: Landslide hazard assessment and historical landslide data—an inseparable couple? In The use of historical data in natural hazard assessments, Springer Netherlands, 153-168 pp., 2001.

Ghirotti, M.: The 1963 Vaiont landslide, Italy. In: J.J. Claque and D. Stead (eds.) Landslides: Types, mechanisms and modeling. Cambridge University Press, NY, 359 PP., 2012.

Godt, J.W., Schulz, W.H., Baum, R.L., and Savage, W.Z.: Modeling rainfall conditions for shallow landsliding in Seattle, Washington, Reviews in Engineering Geology, 20: 137-152, 2008.

Godt, J.W., and McKenna, J.P.: Numerical modeling of rainfall thresholds for shallow landsliding in the Seattle, Washington, area, Reviews in Engineering Geology, 20: 121-136, 2008.

Goode, J.R., Luce, C.H., and Buffington, J.M.: Enhanced sediment delivery in a changing climate in semi-arid mountain basins: Implications for water resource management and aquatic habitat in the northern Rocky Mountains, Geomorphology, 139: 1-15, 2012.

Gorsevski, P.V., Gessler, P.E., Boll, J., Elliot, W.J., and Foltz, R.B.: Spatially and temporally distributed modeling of landslide susceptibility, Geomorphology, 80.3: 178-198, 2006.

Guthrie, R.H., and Brown, J.K.: Denudation and landslides in coastal mountain watersheds: 10,000 years of erosion, Geographica Helvetica, 63(1): 26-35, 2008.

Guthrie, R.H., and Evans, S.G.: Analysis of landslide frequencies and characteristics in a natural system, coastal British Columbia, Earth Surface Processes and Landforms, 29(11): 1321-1339, 2004.

Hales, T.C., Cole-Hawthorne, C., Lovell, L., and Evans, S.L.: Assessing the accuracy of simple field based root strength measurements, Plant and soil, 372(1-2): 553-565, 2013.

Hamlet, A.F., M.M. Elsner, G. Mauger, S. Lee, and Tohver, I.: An Overview of the Columbia Basin Climate Change Scenarios Project: Approach, Methods, and Summary of Key Results, Atmosphere-Oceans, 51(4): 392-415, 2013.

Hammond, C., Hall, D., Miller, S., and Swetik, P.: Level 1 stability analysis (LISA), documentation for Version 2.0. USDA, For. Serv., Moscow, ID, Intermountain Res. Sta. Gen. Tech. Rep. INT-285, 1992.

Hanley, J.A., and McNeil, B.J.: The meaning and use of the area under a receiver operating characteristic (ROC) curve, Radiology, 143(1): 29-36, 1982.

Haugerud, R.A., and Tabor, R.W.: Geologic map of the North Cascade Range, Washington, US Department of the Interior, US Geological Survey, 29 pp., 2009.

Heimsath, A.M., Dietrich, W.E., Nishiizumi, K., and Finkel, R.C.: The soil production function and landscape equilibrium, Nature, 388(6640): 358-361, 1997.

Hobley, D.E.J., Adams, J.M., Nudurupati, S.S., Hutton, E.W.H., Gasparini, N.M., Istanbulluoglu, E., and Tucker, G. E.: Creative computing with Landlab: an open-source toolkit for building, coupling, and exploring two-dimensional numerical models of Earth-surface dynamics, Earth Surf. Dynam., 5(1): 21-46, doi:10.5194/esurf-5-21-2017, 2017.

Horsburgh, J.S., Morsy, M.M., Castronova, A.M., Goodall, J.L., Gan, T., Yi, H., Stealey, M.J., and Tarboton, D. G.: HydroShare: Sharing Diverse Environmental Data Types and Models as Social Objects with Application to the Hydrology Domain, JAWRA Journal of the American Water Resources Association, 52(4): 873-889, http://dx.doi.org/10.1111/1752-1688.12363, 2016.

Hren, M.T., Hilley, G.E., and Chamberlain, C.P.: The relationship between tectonic uplift and chemical weathering rates in the Washington Cascades: field measurements and model predictions, American Journal of Science, 307(9): 1041-1063, 2007.

Idaszak, R., Tarboton, D.G., Yi, H., Christopherson, L., Stealey, M.J., Miles, B., Dash, P., Couch, A., Spealman, C., Ames, D.P., and Horsburgh, J.S.: HydroShare - A case study of the application of modern software engineering to a large distributed federally-funded scientific software development project, Chapter 10 in Software Engineering for Science, Edited by J. Carver, N. P. Chue Hong and G. K. Thiruvathukal, Taylor and Francis CRC Press, 219-236 pp., 2016.

Islam, S.U., Déry, S.J., and Werner, A.T.: Future climate change impacts on snow and water resources of

the Fraser River Basin, British Columbia. Journal of Hydrometeorology, 18: 473-496, doi: http://dx.doi.org/10.1175/JHM-D-16-0012.1, 2017.

Istanbulluoglu, E.: Modeling catchment evolution: from decoding geomorphic processes signatures toward predicting impacts of climate change. Geography Compass, 3(3): 1125-1150, 2009.

Istanbulluoglu, E., Tarboton, D.G., Pack R.T., and Luce, C.H.: Modeling of the interactions between forest vegetation, disturbances, and sediment yields. Journal of Geophysical Research: Earth Surface, 109(F1), 2004.

Istanbulluoglu, E., and Bras, R.L.: Vegetation-modulated landscape evolution: Effects of vegetation on landscape processes, drainage density, and topography, J. Geophys. Res., 110: F02012, doi:10.1029/2004JF000249, 2005.

Iverson, R.M., Reid, M.E., and LaHusen, R.G.: Debris-flow mobilization from landslides, Annual Review of Earth and Planetary Sciences, 25(1): 85-1, 1997.

Iverson, R. M.: Landslide triggering by rain infiltration, Water resources research, 36(7): 1897-1910, 2000.

Jin, S, Yang L, Danielson P, Homer C, Fry J, and Xian, G.: A comprehensive change detection method for updating the National Land Cover Database to circa 2011, Remote Sensing of Environment, 132: 159 175, 2013.

Kirschbaum, D.B., R. Adler, Y. Hong, S. Kumar, C. Peters-Lidard, and Lerner-Lam, A.: Advances in landslide nowcasting: evaluation of global and regional modeling approach. Environ. Earth. Sci. 66: 1683-1696, 2012.

Liang X., Lettenmaier D.P., Wood, E.F., and Burges, S.J.: A simple hydrologically based model of land surface water and energy fluxes for GSMs, J Geophys Res 99(D7): 14,415–14,428, 1994.

Livneh B., Rosenberg, E.A., Lin, C., Nijssen, B., Mishra, V., Andreadis, K.M., Maurer, E.P., and Lettenmaier, D.P.: A Long-Term Hydrologically Based Dataset of Land Surface Fluxes and States for the Conterminous United States: Update and Extensions, Journal of Climate, 26: 9384–9392, 2013.

Livneh B., Bohn, T.J., Pierce, D.S., Munoz-Ariola, F., Nijssen, B., Vose, R., Cayan, D., and Brekke, L.D.: A spatially comprehensive, hydrometeorological data set for Mexico, the U.S., and southern Canada 1950-2013, Nature Scientific Data, 5:150042, doi:10.1038/sdata.2015.42, 2015.

Lee S., Ryu, J-H., and Kim, I-S.: Landslide susceptibility analysis and its verification using likelihood ratio, logistic regression, and artificial neural network models: Case study of Youngin, Korea. Landslides, 4:327–338, 2007.

Legg, N.T., Meigs, A.J., Grant, G.E., and Kennard, P.: Debris flow initiation in proglacial gullies on Mount Rainier, Washington, Geomorphology, 226, 249-260, 2014.

Löffler, J.: The influence of micro-climate, snow cover, and soil moisture on ecosystem functioning in high mountains, Journal of Geographical Sciences, 17(1), 3-19, 2007.

Lu, N., and Godt, J.W.: Hillslope hydrology and stability, Cambridge University Press, 2013.

May, C.L., Pryor, B., Lisle, T.E., and Lang, M.: Coupling hydrodynamic modeling and empirical measures of bed mobility to predict the risk of scour and fill of salmon redds in a large regulated river, Water Resources Research 45, W05402, 2009.

Miller D.J.: Coupling GIS with physical models to assess deep-seated landslide hazards, Environ. Eng. Geosci., 1(3): 263–276, 1995.

Mancini, F., Ceppi, C., and Ritrovato, G.: GIS and statistical analysis for landslide susceptibility mapping in the Daunia area, Italy, Natural Hazards and Earth System Sciences, 10(9): 1851, 2010.

Mitchell, S.G., and Montgomery, D.R.: Influence of a glacial buzzsaw on the height and morphology of the Cascade Range in central Washington State, USA. Quaternary Research, 65(1): 96-107, 2006.

Molnar, P.: Late Cenozoic increase in accumulation rates of terrestrial sediment: How might climate change have affected erosion rates?, Annu. Rev. Earth Planet. Sci., 32, 67-89, 2004.

Montgomery, D.R.: Slope distributions, threshold hillslopes, and steady-state topography. American Journal of science, 301(4-5), 432-454, 2001.

Montgomery, D.R. and Dietrich, W.E.: A Physically Based Model for the Topographic Control on Shallow Landsliding, Water Resources Research, 30(4): 1153-1171, 1994.

Montgomery, D.R., and Foufoula-Georgiou, E.: Channel network source representation using digital elevation models. Water Resources Research, 29(12): 3925-3934, 1993.

Montrasio, L., and Valentino, R.: Modelling Rainfall-induced Shallow Landslides at Different Scales Using SLIP-Part I. Procedia Engineering, 158: 476-481, 2016.

Moon, S., Chamberlain, C.P., Blisniuk, K., Levine, N., Rood, D.H., and Hilley, G.E.: Climatic control of denudation in the deglaciated landscape of the Washington Cascades, Nature Geoscience, 4(7): 469-473, 2011.

Morsy, M.M., Goodall, J.L., Castronova, A.M., Dash, P., Merwade, V., Sadler, J.M., Rajib, M.A., Horsburgh, J.S., and Tarboton, D.G.: Design of a metadata framework for environmental models with an example hydrologic application in HydroShare, Environmental Modelling & Software, 93: 13-28, http://dx.doi.org/10.1016/j.envsoft.2017.02.028, 2017.

Naudet, V., Lazzari, M., Perrone, A., Loperte, A., Piscitelli, S., and Lapenna, V.: Integrated geophysical and geomorphological approach to investigate the snowmelt-triggered landslide of Bosco Piccolo village (Basilicata, southern Italy), Engineering Geology, 98(3): 156-167, 2008.

Nadim, F., Kjekstad, O., Peduzzi, P., Herold, C., and Jaedicke, C.: Global landslide and avalanche hotspots, Landslides, 3(2): 159-173, 2006.

Nicótina, L., Tarboton, D. G., Tesfa, T. K., and Rinaldo, A.: Hydrologic controls on equilibrium soil depths, Water Resources Research, 47(4), 2011.

Nimmo, J.R.: Unsaturated Zone Flow Processes, in Anderson, M.G., and Bear, J., eds., Encyclopedia of HydrologicalSciences: Part 13--Groundwater: Chichester, UK, Wiley, v. 4, p. 2299-2322, doi:10.1002/0470848944.hsa161, 2005.

Okimura, T.: Prediction of slope failure using the estimated depth of the potential failure layer, J. Natural Disaster Sci., 11(1):67-89, 1989.

O'loughlin, E. M.: Prediction of surface saturation zones in natural catchments by topographic analysis. Water Resources Research, 22(5): 794-804, 1986.

Pack, R.T., Tarboton, D.G., and Goodwin, C.: SINMAP 2.0-A Stability Index Approach to Terrain Stability Hazard Mapping, User's Manual. Available online: http://www.engineering.usu.edu/dtarb/sinmap.html [Accessed 30 Jan. 1916], 2005.

Pack, R.T., D.G. Tarboton, and Goodwin, C.N.: Assessing Terrain Stability in a GIS using SINMAP, 15th Annual GIS Conference, Vancouver: http://hydrology.usu.edu/sinmap/gis2001.pdf, 2001.

Pack R.T., Tarboton, D.G., and Goodwin, C.N.: The SINMAP approach to terrain stability mapping. In: Proceedings of the 8th international congress of the international association of engineering geology and the environment, Vancouver, British Columbia, Canada, September 21–25, vol 2. AA Balkema, Rotterdam, pp 1157–1165, 1998.

Page, M.J., Trustrum, N.A., and DeRose, R.C.: A high-resolution record of storm-induced erosion from lake sediments, New Zealand, Journal of Paleolimnology, 11: 333-348, 1994.

Pardeshi, S.D., Autade, S.E., and Pardeshi, S.S.: Landslide hazard assessment: recent trends and techniques, SpringerPlus, 2(1): 523, 2013.

Pelletier, J.D., Barron-Gafford, G.A., Breshears, D.D., Brooks, P.D., Chorover, J., Durcik, M., Harman, C.J., Huxman, T.E., Lohse, K.A., Lybrand, R. and Meixner, T.: Coevolution of nonlinear trends in vegetation, soils, and topography with elevation and slope aspect: a case study in the sky islands of southern Arizona, Journal of Geophysical Research-Earth Surface, 118: 741–58, 2013.

Pelletier, J.D., and Rasmussen, C.: Geomorphically based predictive mapping of soil thickness in upland

watersheds, Water Resources Research, 45(9): W09417, doi:10.1029/2008WR007319, 2009.
Pollok, M.M.: Biodiversity, In: R. J. Naiman and R. E. Bilby (eds.) River Ecology and Management: Lessons from the Pacific Coastal Ecoregion, Springer-Verlag, New York, 430–452 pp., 1998.
PRISM Climate Group: Oregon State University, http://prism.oregonstate.edu, created 4 Feb 2004.
Raia S, Alvioli M, Rossi M, Baum RL, Godt JW, and Guzzetti, F.: Improving predictive power of physically based rainfall-induced shallow landslide models: A probabilistic approach, Geosci Model Dev Discuss, 6:1367–1426, 2014.
Regmi, N.R., Giardino, J.R., McDonald, E.V., and Vitek, J.D.: A comparison of logistic regression-based models of susceptibility to landslides in western Colorado, USA. Landslides, 11(2): 247-262, 2014.
Reiners, P.W., Ehlers, T.A., Mitchell, S.G., and Montgomery, D.R.: Coupled spatial variations in precipitation and long-term erosion rates across the Washington Cascades, Nature, 426(6967), 645-647, 2003.
Reiners, P.W., Ehlers, T.A., Garver, J.I., Mitchell, S.G., Montgomery, D.R., Vance, J.A., and Nicolescu, S.: Late Miocene exhumation and uplift of the Washington Cascade Range, Geology, 30(9): 767-770, 2002.
Richards, L.A.: Capillary conduction of liquids in porous mediums, Physics, 1, 318–333, 1931.
Riedel, J, Brady S, Dorsch S, and Wegner, J.: Geomorphology of the Thunder Creek Watershed: Landform Mapping at North Cascades National Park Service Complex, Washington. Natural Resource Technical Report NPS/NCCN/NRTR—2012/567. National Park Service, Fort Collins, Colorado, 2015.
Riedel, J, and Probala, J.: Mapping ecosystems at the landform scale in Washington state, Park Science 23-2: 37-42, 2005.
Roe, G.H.: Orographic Precipitation. Annu. Rev. Earth Planet. Sci., 33:645–71, 2005.
Roering, J.J.: Soil creep and convex-upward velocity profiles: Theoretical and experimental investigation of disturbance-driven sediment transport on hillslopes, Earth Surface Processes and Landforms, 29(13): 1597-1612, 2004.
Roering, J.J., Schmidt, K.M., Stock, J.D., Dietrich, W.E., and Montgomery, D.R.: Shallow landsliding, root reinforcement, and the spatial distribution of trees in the Oregon Coast Range, Canadian Geotechnical Journal, 40(2): 237-253, 2003.
Roering, J.J., Kirchner, J.W., and Dietrich, W.E.: Evidence for nonlinear, diffusive sediment transport on hillslopes and implications for landscape morphology, Water Resources Research, 35(3): 853-870. 1999.
Schmidt, K.M., Roering, J.J., Stock, J.D., Dietrich, W.E., Montgomery, D.R., and Schaub, T.: The variability of root cohesion as an influence on shallow landslide susceptibility in the Oregon Coast Range, Canadian Geotechnical Journal, 38(5), 995-1024, 2001.
Selby, M.J.: Hillslope Materials and Processes. 2nd edit., Oxford University Press, 1993.
Sidle, R.C.: A conceptual model of changes in root cohesion in response to vegetation management, Journal of Environmental Quality, 20(1): 43-52, 1991.
Sidle, R.C.: A theoretical model of the effects of timber harvesting on slope stability, Water Resources Research, 28(7): 1897-1910, 1992.
Sidle, R.C., Noguchi, S., Tsuboyama, Y., and Laursen, K.: A conceptual model of preferential flow systems in forested hillslopes: Evidence of self-organization, Hydrological Processes, 15(10): 1675-1692, 2001.
Sidle, R.C., and Ochiai, H.: Landslides: processes, prediction, and land use, Water Resources Monogram 18, American Geophysical Union, Washington DC, 2006.
Smith, K.: Mass movement hazards (Ch. 8), In: Environmental hazards: Assessing risk and reducing disasters (6th edition). Routledge, New York, NY., 205-234 pp., 2013.
Strenk, P.M.: Evaluation of analytical procedures for estimating seismically induced permanent

deformations in slopes, Doctoral Thesis, Dexel University, 2010.

Stock, J., and Dietrich, W.E.: Valley incision by debris flows: Evidence of a topographic signature, Water Resources Research 39.4, 2003.

Strauch, R., E. Istanbulluoglu, S. S. Nudurupati, C. Bandaragoda (2017). Regional landslide hazard using Landlab - NOCA Data, HydroShare, http://www.hydroshare.org/resource/a5b52c0e1493401a815f4e77b09d352b

Sweeney, K.E., Roering, J.J., and Ellis, C.: Experimental evidence for hillslope control of landscape scale. Science, 349(6243), 51-53, 2015.

Tarboton, D.G., Idaszak, R., Horsburgh, J.S., Heard, J., Ames, D., Goodall, J.L., Band, L., Merwade, V., Couch, A., Arrigo, J., Hooper, R., Valentine, D., and Maidment, D.: HydroShare: Advancing Collaboration through Hydrologic Data and Model Sharing, in D. P. Ames, N. W. T. Quinn and A. E. Rizzoli (eds), Proceedings of the 7th International Congress on Environmental Modelling and Software, San Diego, California, USA, International Environmental Modelling and Software Society (iEMSs), ISBN: 978-88-9035-744-2, 2014. http://www.iemss.org/sites/iemss2014/papers/iemss2014_submission_243.pdf, 2014.

Tarolli, P., Borga, M., and Dalla Fontana, G.: Analysing the influence of upslope bedrock outcrops on shallow landsliding, Geomorphology, 93(3): 186-200, 2008.

Tarolli, P., and Dalla Fontana, G.: Hillslope-to-valley transition morphology: new opportunities from high resolution DTMs, Geomorphology, 113(1), 47-56, 2009.

Tarolli, P. and Tarboton, D.G.: A new method for determination of most likely landslide initiation points and the evaluation of digital terrain model scale in terrain stability mapping, Hydrol. Earth Syst. Sci. 10: 663-677, 2006.

Taylor, F., and Brabb, E.E.: Map showing the status of landslide inventory and susceptibility mapping in California (No. 86-100). US Geological Survey,1986.

Tesfa, T.K., Tarboton, D.G., Chandler, D.G., and McNamara, J.P.: Modeling soil depth from topographic and land cover attributes. Water Resources Research, 45(10), 2009.

Tobutt D.C.: Monte Carlo simulation methods for slope stability. Comput. Geosci., 8(2): 199–208, 1982.

Tucker, G.E., Hobley, D.E., Hutton, E.W.H., Gasparini, N.M., Istanbulluoglu, E., Adams, J.M., and Nudurupati, S.S.: CellLab-CTS 2015: a Python library for continuous-time stochastic cellular automaton modeling using Landlab., Geoscientific Model Development, 8: 9507-9552, doi:10.5194/gmd-9-823-2016, 2016.

Tucker, G.E., and Bras, R.L.: Hillslope processes, drainage density, and landscape morphology. Water Resources Research, 34(10), 2751-2764, 1998.

Tucker, G.E., and Slingerland, R.: Drainage basin responses to climate change. Water Resources Research, 33(8), 2031-2047, 1997.

United States Department of the Interior, National Park Service (DOI-NPS).: Foundation Document, North Cascades National Park Complex, Washington. Available from: https://www.nps.gov/noca/learn/management/upload/North-Cascades-NP-Complex-Foundation-Document_small.pdf (Accessed 23 January 2017), 2012.

U.S. Department of Agriculture, Natural Resources Conservation Service (DOA-NRCS), and United States Department of the Interior, National Park Service (DOI-NPS).: Soil survey of North Cascades National Park Complex, Washington, 2012.

United States Department of Agriculture, Natural Resources Conservation Service (DOA-NRCS).: United States Department of Agriculture. Web Soil Survey. Available from: http://websoilsurvey.nrcs.usda.gov/. (Accessed 23 January 2017), 2016.

DOA-NRCS.: Soil Data Viewer software. Available from: www.nrcs.usda.gov/wps/portal/nrcs/detailfull/soils/home/?cid=nrcs142p2_053620 [Accessed 23

June 1915], 2015a.

DOA-NRCS.: Soil Texture Calculator software. Available from: www.nrcs.usda.gov/wps/portal/nrcs/detail/soils/survey/?cid=nrcs142p2_054167 [Accessed 24 June 1915], 2015b.

United States Geological Survey (USGS).: Shuttle Radar Topography Mission (STRM) 1 arc-second global, Joint NASA-NGA partnership, data distributed and archived by USGS EROS Data Center, Available online at https://lta.cr.usgs.gov/SRTM1Arc. (Accessed 26 April 2017), 2017.

USGS.: National Elevation Data last modified March 6, 2014, National Map Viewer (Accessed 24 November 2014), 2014a.

USGS.: National Land Cover Data (NLCD) version Marched 31, 2014, National Map Viewer (Accessed 25 November 2014), 2014b.

Van Westen, C.J., Van Asch, T.W., and Soeters, R.: Landslide hazard and risk zonation—why is it still so difficult? Bulletin of Engineering geology and the Environment, 65(2), 167-184, 2006.

Van Beek, L.P.H.: Assessment of the influence of changes in land use and climate on landslide activity in a Mediterranean environment (Doctoral dissertation), Nederlandse Georafische Studies, Universiteit Utrecht. pp 294, 2002.

Yin, D., Liu, Y.Y., Padmanabhan, A., Terstriep, J., Rush, J., and Wang, S.: A CyberGIS-Jupyter Framework for Geospatial Analytics at Scale. The First Practice & Experience in Advanced Research Computing (PEARC) Conference, Under review, 2017.

Wayand, N., Stimberis, J., Zagrodnik, J., Mass, C.F. and Lundquist, J.D.: Improving Simulations of Precipitation Phase and Snowpack at a Site Subject to Cold Air Intrusions: Snoqualmie Pass, WA, J. of Geophysical Research, Atmospheres, 121, doi: 10.1002/2016JD025387, 2016.

Wartman, J., Montgomery, D.R., Anderson, S.A., Keaton, J.R., Benoît, J., dela Chapelle, J., and Gilbert, R.: The 22 March 2014 Oso landslide, Washington, USA. Geomorphology, 253: 275-288, 2016.

Wu, W. and Sidle, R.C.: A Distributed Slope Stability Model for Steep Forested Watersheds, Water Resour. Res., 31(8): 2097– 2110, 1995.

Zizioli, D., Meisina, C., Valentino, R., and Montrasio, L.: Comparison between different approaches to modeling shallow landslide susceptibility: a case history in Oltrepo Pavese, Northern Italy, Natural Hazards and Earth System Sciences 13(3): 559, 2013.